UCRL-16003

University of California

Ernest O. Lawrence Radiation Laboratory

A MEASUREMENT OF THE RELATIVE BRANCHING RATIO $\frac{K^+ \to \mu^+ + \nu}{K^+ \to \pi^+ + \pi^0}$

Berkeley, California

3 to

DISCLAIMER

Special Thesis

UCRL-16003

UNIVERSITY OF CALIFORNIA
Lawrence Radiation Laboratory
Berkeley, California

A MEASUREMENT OF THE RELATIVE BRANCHING RATIO $\frac{K^+ \to \mu^+ + \nu}{K^+ \to \pi^+ + \pi^0}$

Robert Lamar Beck

(Ph. D. Thesis)

July 28, 1966

A MEASUREMENT OF THE RELATIVE BRANCHING RATIO $\frac{K^+ \to \mu^+ + \nu}{K^+ \to \pi^+ + \pi^0}$

Table of Contents

A MEASUREMENT OF THE RELATIVE BRANCHING RATIO $\frac{K^+ \to \mu^+ + \nu}{K^+ \to \pi^+ + \pi^0}$

Robert Lamar Beck

Lawrence Radiation Laboratory
University of California
Berkeley, California

July 28, 1966

ABSTRACT

K^+ - mesons in a momentum-analyzed beam were identified by a velocity selecting Čerenkov counter and brought to rest in a beryllium target which served as a source for a broad-range magnetic spectrometer. Muons and pions from the decay modes

$$K^+_{\mu 2} \to \mu^+ + \nu \qquad P_\mu = 236 \text{ MeV/c}$$

and

$$K^+_{\pi 2} \to \pi^+ + \pi^0 \qquad P_\pi = 205 \text{ MeV/c}$$

were identified by momentum and range, and a value $2.31 \pm .24$ for the relative branching ratio $K\mu 2/K\pi 2$ was obtained. The value is compared with results of other experiments.

I. INTRODUCTION

The principal decay modes of the charged K meson are listed in Table I. Other decay modes have been observed, but because of their small branching ratios these modes will not concern us here.

The scatter in the measured $K\pi 2$ and $K\mu 2$ branching ratios has been noted by several authors,[1,7,8] and has even led to speculation that the differences between the xenon bubble chamber results and the results of experiments 1, 2, and 3 of Table I may have some physical basis.* However, it can be seen that the second xenon $K\pi 2$ branching ratio (experiment 6) agrees well with experiments 1 and 3 of Table I, and does not disagree strongly with experiment 2. At the same time it does not agree at all with the first xenon $K\pi 2$ branching ratio. Shaklee et al.[6] indicate that the discrepancy is connected with the difficulty of separating the $K\pi 2$ and $K\mu 3$ modes, and believe that the discrepancy in the two xenon results reflects a systematic error in the experiment of Roe et al. Additional information on the $K\pi 2$ mode is provided by a recent measurement by Callahan and Cline, who obtain a branching ratio of $(21.0 \pm .6)$[20], consistent with the second xenon

---

*The xenon experiments distinguished the $K\pi 2$ from the $K\mu 2$ mode by identifying the π^0 γ-ray conversions, whereas experiments 1, 2, and 3 identified these modes by following the charged secondary particle. Goldberg and Landovitz[7] and Everett[8] postulate a decay mode $K^+ \to \pi^+ + x$ where x is a stable neutral meson (or "shadow pion") of mass m_π, which would resolve the apparent discrepancy between the xenon two-body branching ratios and 1, 2, and 3 of Table I. The xenon experiments would identify this decay as $K\mu 2$, while the other experiments would class it with the $K\pi 2$.

Table I

Decay Mode	Becker[1]	Birge[2]	Alexander[3]	Taylor[4]	Roe[5]	Shaklee[6]	Callahan[20]
$K\mu 2 \to \mu^+ + \nu$	57.5 ± 3.8	58.5 ± 3.0	56.9 ± 2.6		64.2 ± 1.3	63.0 ± 0.8	
$K\pi 2 \to \pi^+ + \pi^0$	25.0 ± 3.3	27.7 ± 2.7	23.2 ± 2.2		18.6 ± 0.9	22.4 ± 0.8	21.0 ± 0.6
$K\mu 3 \to \mu^+ + \pi^0 + \nu$		2.8 ± 1.0	5.9 ± 1.3	2.8 ± 0.4	4.8 ± 0.6	3.0 ± 0.5	
$Ke3 \to e^+ + \pi^0 + \nu$	11.8 ± 2.0	3.2 ± 1.3	5.1 ± 1.3		5.0 ± 0.5	4.7 ± 0.3	
$\tau^{+\prime} \to \pi^+ + 2\pi^0$		2.1 ± 0.5	2.2 ± 0.4	1.5 ± 0.2	1.7 ± 0.2	1.8 ± 0.2	
$\tau^+ \to 2\pi^+ + \pi^-$	5.7 ± 0.9	5.6 ± 0.4	6.8 ± 0.4	5.2 ± 0.3	5.7 ± 0.3	5.1 ± 0.2	
$K\mu 2/K\pi 2$	2.30± .34	2.11± .22	2.45± .25		3.45± .18	2.81± .11	

[1] Helium Bubble Chamber (K^-)

[2,3,4] Nuclear Emulsion (K^+)

[5,6] Xenon Bubble Chamber (K^+)

[20] Freon Bubble Chamber (K^+)

result, but not with the first. The models proposed in references 7 and 8 appear to be rulled out by this experiment, since it identified the $K\pi2$ by observation of the π^+. It should also be noted that this last $K\pi2$ ratio differs by only 1.2 standard deviations from that of Becker et al., and therefore does not support the contention[20] that the $K\pi2^+$ and $K\pi2^-$ branching ratios are consistent.

The objectives of the experiment reported here were the measurement of the momentum dependence of the Ke3 and $K\mu3$ charged spectra above 100 MeV/c and their partial branching ratios relative to the $K\mu2/K\pi2$. Identification of these modes was to be made on the basis of range (pions vs. muons) and velocity (muons vs. positrons) in a threshold Cerenkov counter. However, limitations imposed by background contaminations and low counting rates made it impossible to determine the Ke3 and $K\mu3$ spectra clearly.

We report here a measurement of the relative branching ratio $K\mu2/K\pi2$. The $K\pi2$ pion and $K\mu2$ muon were identified by momentum and range. In outline the report consists of a description of the experimental method and equipment, analysis of data, and a discussion of calculated corrections to the observed $K\mu2/K\pi2$ ratio.

II. EXPERIMENTAL METHOD AND EQUIPMENT

A. Beam Layout

The K beam layout is shown in Figure 1. The internal Bevatron production target was of tungsten alloy, 3 x 1/2 x 1/4 inches, located in the west straight section of the Bevatron. Positive particles produced at 26^{o} to the circulating internal proton beam of approximately 10^{11} protons per pulse entered the K beam channel after passing through a thin window in the vacuum tank of the Bevatron. The beam was momentum analyzed by M1, a 16" x 36" C magnet, with eight inch gap, and brought to a first focus inside the field lens S by the action of Q1, a quadrupole doublet with dimensions 8" x 16" x 16". S was a quadrupole singlet, also 8" x 16" x 16".

The second half of the beam system was a mirror image of the first, and produced a final focus just before the Cerenkov counter, which provided electronic separation between K mesons and other particles in the beam. Vertical horizontal beam profiles measured 1 foot downstream from the Cerenkov counter are shown in Figure 2.

After leaving the Cerenkov counter, the beam particles passed through a thickness of copper degrader sufficient to bring the K mesons to rest in a beryllium-scintillator target sandwich located at the source position of a broad-range magnetic spectrometer. The particle flux into this target was approximately 50,000 π's and 300 K's per pulse.

B. Cerenkov Counter

The Cerenkov counter used to identify K mesons in the beam is shown in sectional view in Figure 3. The section is along the diagonal

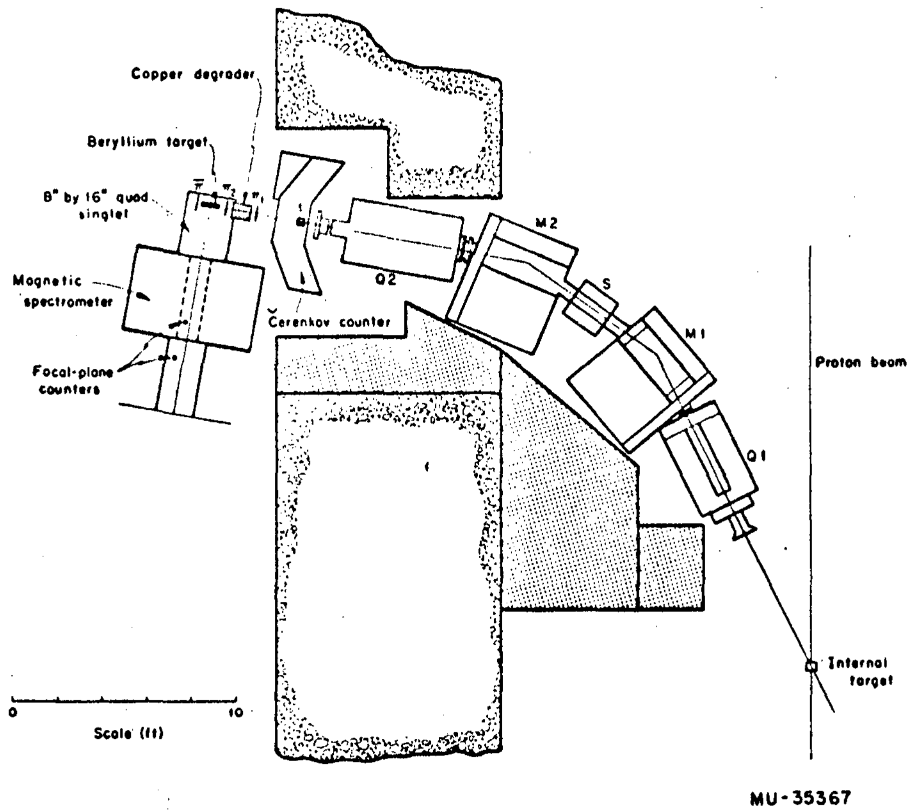

Fig. 1. Beam Layout

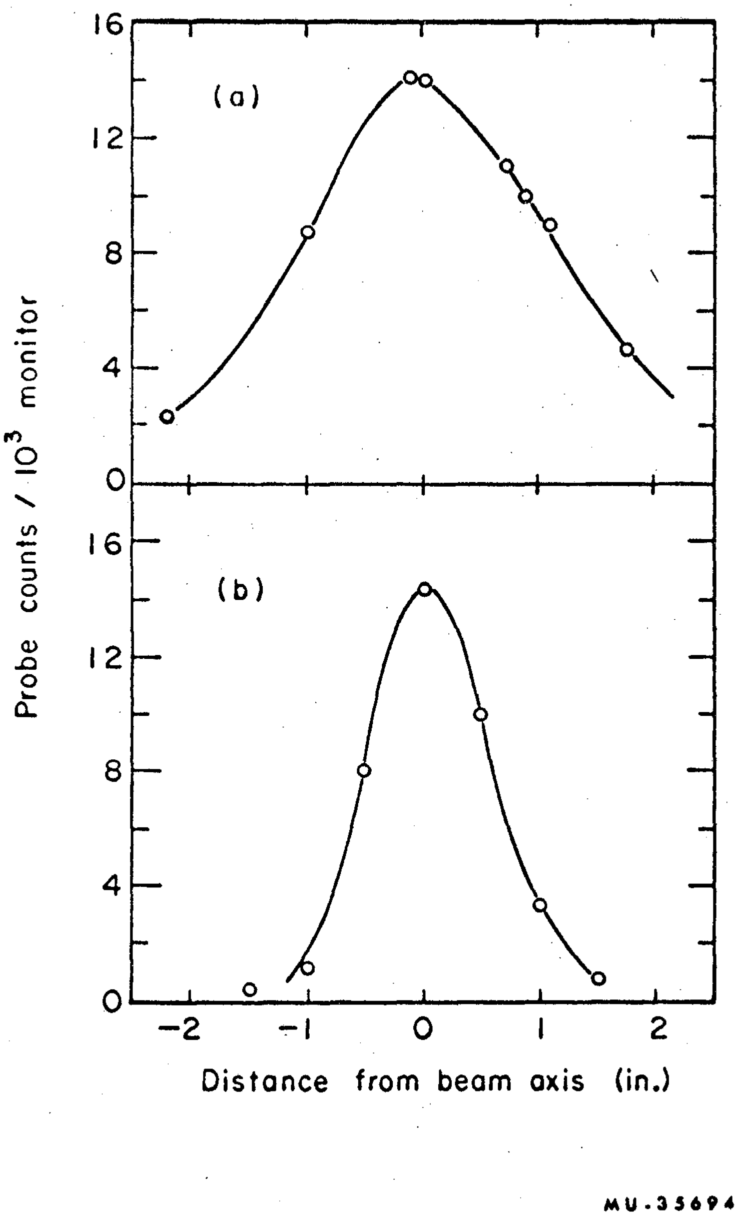

Fig. 2. Horizontal and vertical profiles of beam.

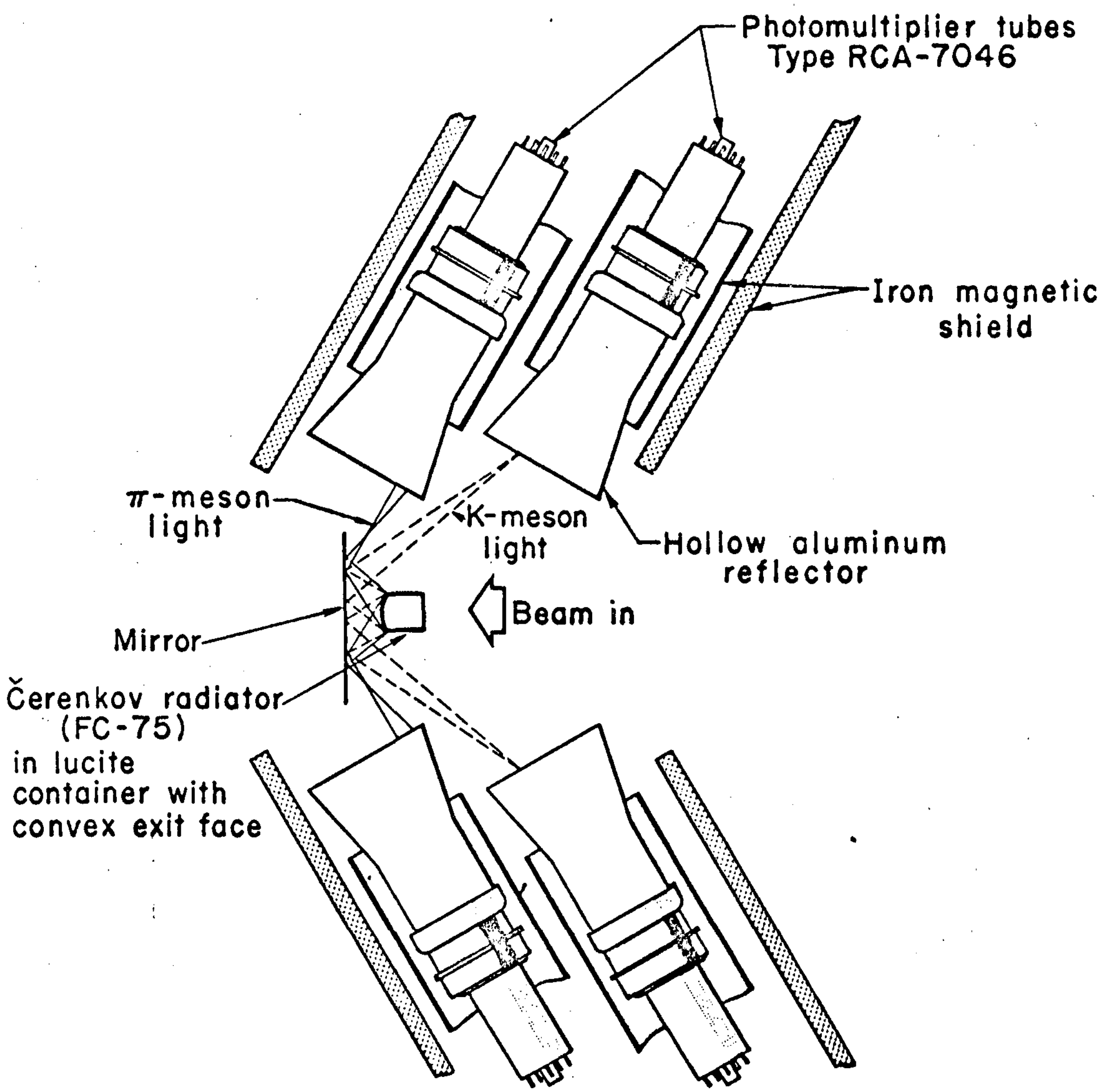

MUB-648-A

Fig. 3. Section through Cerenkov counter

of a hexagon; the complete counter consists of three such sections, symmetrically disposed around the beam axis at 120^{o} to one another. The Cerenkov radiator was liquid Fluorochemical (FC-75) in a cylindrical lucite container. The exit face of the radiator had positive curvature, of 8 inch radius. A particle of velocity β traversing the radiator produced a cone of Cerenkov light of half angle $\Theta = \cos^{-1} 1/n\beta$ where n is the refractive index of FC-75 (n = 1.28). The light produced by K mesons left the exit end of the radiator and was refracted to a wider angle determined by the curvature of the exit face. This light was reflected from a plane mirror and was then transmitted by specular reflection down an aluminum light pipe to the photocathode of an RCA 7046 photomultiplier tube. Light leaving the radiator at a greater angle (corresponding to a lighter particle at that momentum) was prevented from entering this light pipe by a circular aluminum baffle (not shown). The light from pions of the same momentum was directed into a similar ring of phototubes, as shown in the figure. Hence the six phototubes in the ring on the downstream side of the Cerenkov counter viewed pions, while the six upstream phototubes were positioned in the K meson light cone.

The phototubes in the K meson ring were divided into two groups by adding the signals from alternate tubes around the ring. A coincidence between these two groups was required for the K "yes" signal - i.e., two non-adjacent phototubes in the K ring were required in coincidence for the K identification. The pion anticoincidence signal was obtained by adding all six channels in the pion ring; hence a signal from any pion phototube provuded a "no" signal, thereby rejecting that particle.

Figure 4 is a plot of the counting rate in the K meson channel versus radiator position.

C. Electronics

Figure 5 is a simplified schematic drawing of the electronics used in this experiment. With the exception of the target and beam-monitor telescopes, the positions of all counters are shown in Figures 1 and 6. With the exception of the beam Cerenkov counter, all the counters shown in Figures 1 and 2 are standard UCRL plastic scintillators, viewed by RCA 6810A photomultiplier tubes. The target-monitor telescope counters T1, T2, and T3 were located in the shielding wall of the Bevatron and viewed the internal target at 90^{o} to the proton beam direction. The coincidence rate in this telescope provided a measure of the proton flux incident on the internal target. Counters M1 and M2 were located on opposite sides of the beam Cerenkov counter and served to minitor the rate in the secondary beam channel.

The Cerenkov counter has already been described. The two "yes" signals from the K^+ light channel were put into separate coincidence channels of modified Garwin coincidence circuit[9], and the "no" signal was put into an anticoincidence channel of this circuit. All other coincidence circuits shown in Figure 4 were the fast 3-channel coincidence-anticoincidence units designed by Wenzel.[9]

A "target-stop" was defined by the coincidence π_1, π_2, $\overline{\pi}_3$. The output from this coincidence unit was put into a coincidence channel in the Garwin coincidence circuit. The beryllium target sandwich is described in Sections II-D. A1 is the last target dividing scintillator

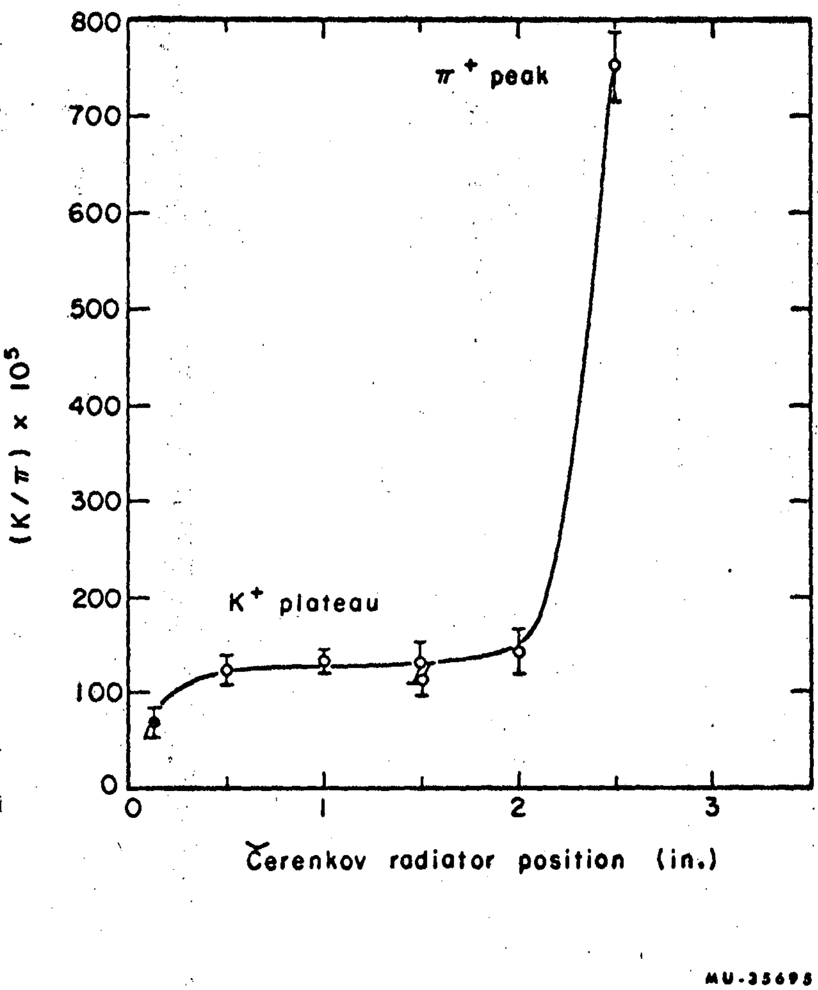

Fig. 4. Counting rate in Cerenkov counter versus radiator position. K^+ mesons were selected by fixing the radiator at the center of the plateau in this curve.

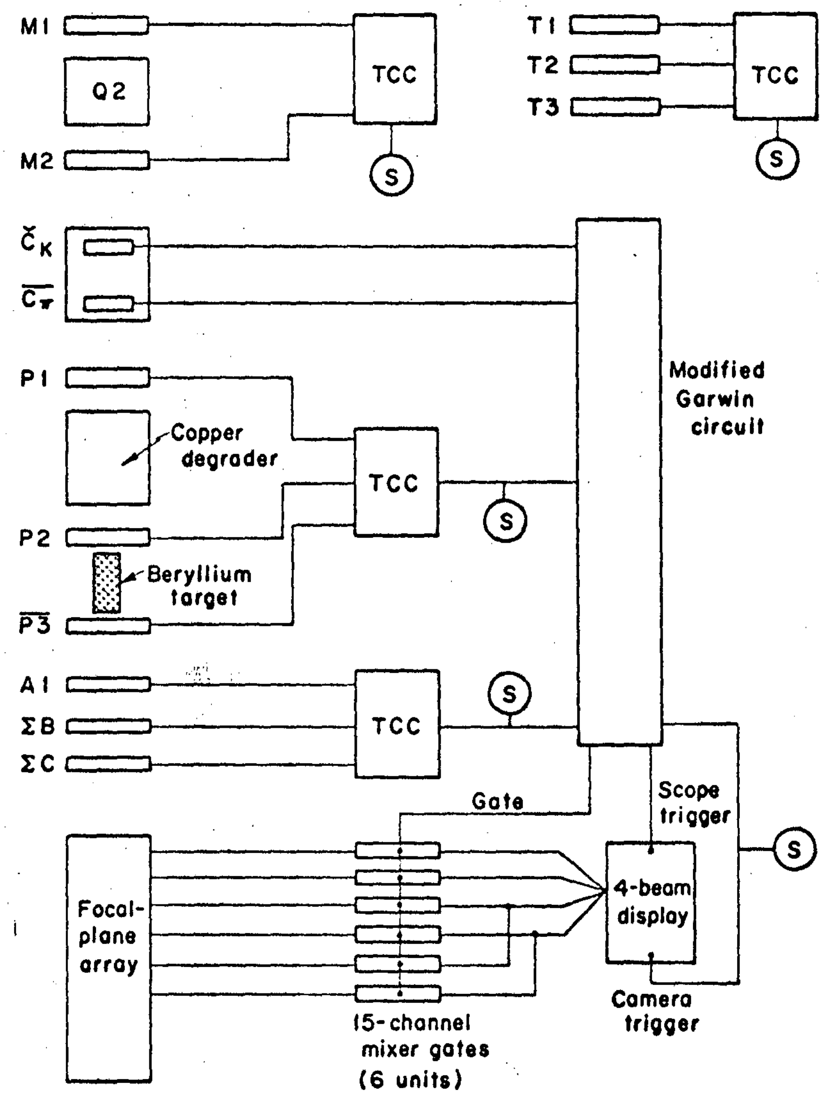

Fig. 5. Simplified schematic of the electronics system.

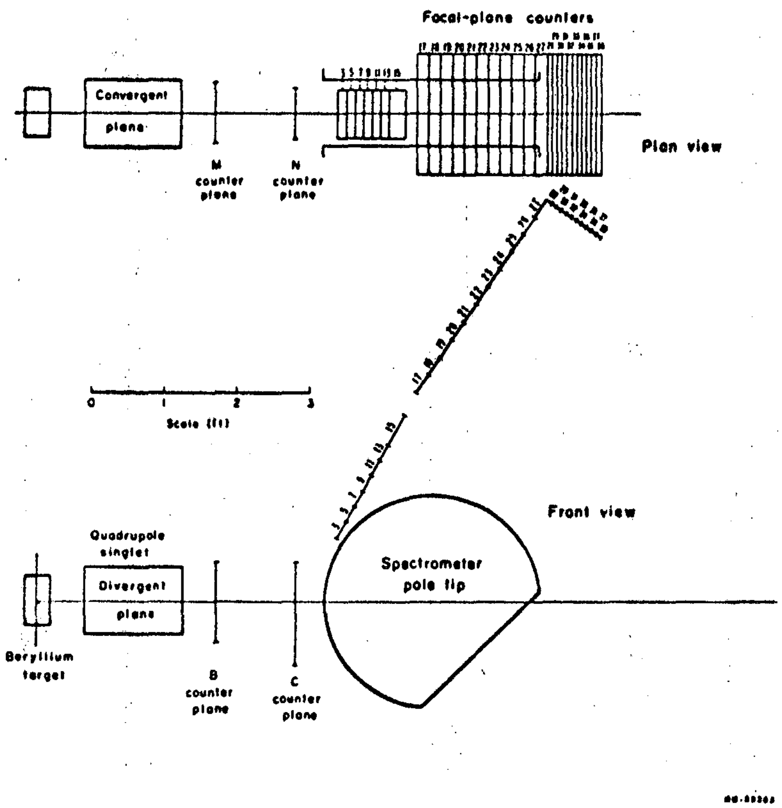

Fig. 6. The broad-range magnetic spectrometer and counter array.

on that side of the target which faced the magnetic spectrometer. ΣB and ΣC represent the outputs of active adder units into which all B and C plane counter signals were put.

The coincidence A1 $\Sigma B \Sigma C$ indicated that a charged particle had entered the spectrometer.

The requirement for an output pulse from the Garwin circuit was therefore the coincidence

$$C_K \overline{C}_\pi \times \pi 1 \pi 2 \pi \overline{3} \times A1\ \Sigma B \Sigma C$$

This output pulse was used to open a gate to the six 15-channel mixer-gate circuits[10], through which were routed the outputs from all the counters associated with the braod range magnetic spectrometer. The output of each channel of each mixer gate circuit was fed into a continuous 50 ohm transmission line, with 50 nanoseconds delay between adjacent channels to provide separation of the pulses on the oscilloscope display. The outputs of all six mixer gate units were displayed and photographed on a Tektronix 517 modified 4-beam oscilloscope. The oscilloscope and camera triggers were derived from the negative coincidence output of the Garwin circuit, and the mixer gate signal from the positive Garwin output.

D. Broad Range Magnetic Spectrometer

Figure 6 shows the broad-range magnetic spectrometer used to analyze the decay products of the stopped K^+ mesons. The spectrometer consisted of a standard UCRL "H" magnet (Atlas) in which the conventional 18 x 36 inch rectangular pole pieces were replaced by circular pole pieces of 18 inch radius. In addition, a quadrupole singlet lens,

lens, 16 inches long with 8 inch bore, was attached as shown in the figure. The theory of this spectrometer has been extensively discussed in the literature,[11,12,13] and only a brief description will be given here.

Figure 7 is a schematic diagram of the spectrometer, drawn to illustrate the focal properties. In this figure the field is taken to be uniform within the radius R, and zero outside this radius. Use of the quadrupole lens to increase the effective solid angle of the spectrometer was suggested by Enge.[12] The net increase of solid angle in this spectrometer is approximately a factor of three. Analysis of the idealized spectrometer of Figure 7 leads to the following results:

a. The focal surface of the spectrometer is a segment of a hyperbola. In order for the focal point to be at a finite distance and outside the effective field region, the radius of curvature of the particle orbit must lie between $\frac{R}{\sqrt{3}}$ and $R\sqrt{3}$; i.e., the momentum band accepted by the spectrometer is given by $\Delta P = P_o(\sqrt{3} - \frac{1}{\sqrt{3}})$ where P_o is the momentum of that orbit which is deflected through 90^o.

b. The magnification along the focal surface is less than unity, and greater than unity in the axial direction, thus necessitating the use of wide detectors.

The resolution of the spectrometer was limited in fact by the dimensions of the source and the detectors; primarily the former. The source dimensions were dictated by the requirement of a useful K stopping rate in the beryllium target sandwich. In designing this target three considerations had to be weighed:

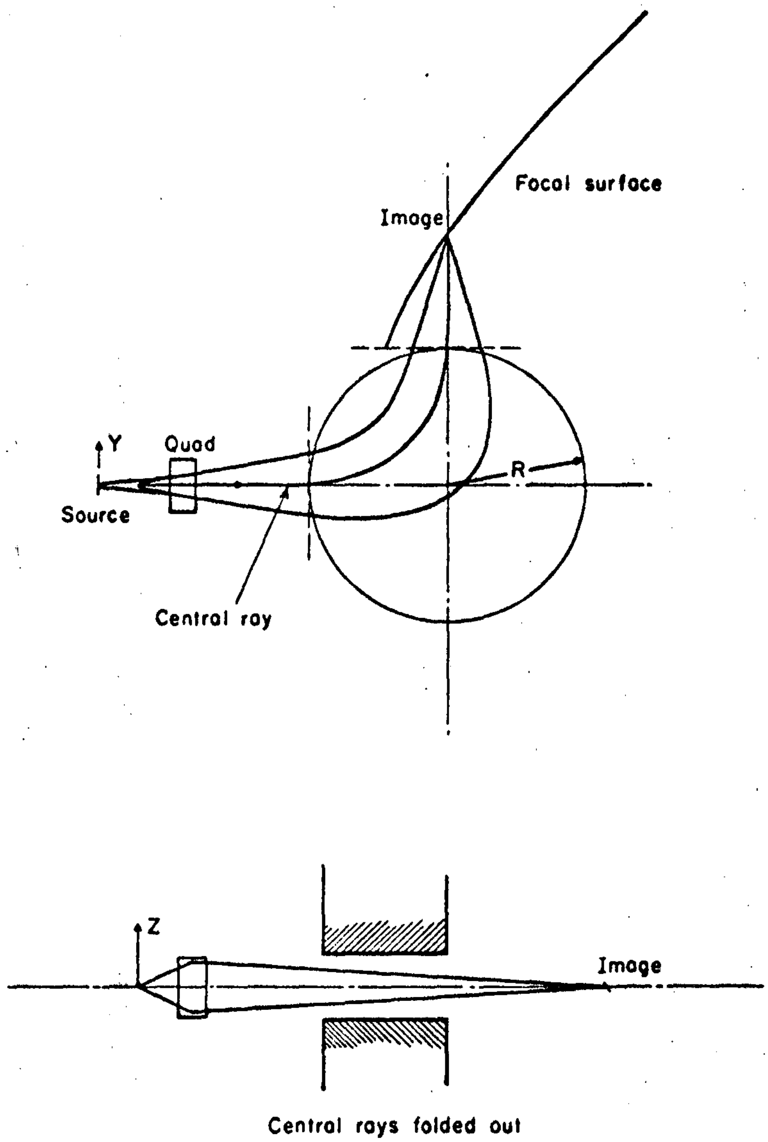

Fig. 7. Illustration of focal properties of spectrometer.

a. The yield of K mesons from the internal Bevatron target is greater at higher take-off momenta.

b. Losses by decay in flight are less at higher momenta

c. Higher K beam momenta would require a greater thickenss of degrader before the beryllium target, increasing the loss of K's by nuclear attenuation.

Preliminary calculations indicated an optimum K stopping rate for a beam momentum of 800-1000 MeV/c, and in the tuneup phase of the experiment this rate was found to be optimum at 950 MeV/c. At this momentum, eleven inches of copper degrader were required to slow the K mesons sufficiently to bring them at rest in the beryllium target. Figure 9 shows the stopping rate in the beryllium target as a function of thickness of degrader. Since the beam leaving such a thickness of copper is spatially diffused, and considerably smeared in momentum, the beryllium target slices were made 8 inches high and 8 inches in the beam direction. The target was made of ten such slices, 200 mils thick, spearated by scintillators 8 x 8 x 1/16 inches. These target-sub-dividing scintillators (denoted as A1 through A10) made it possible to correct the decay events for momentum losses in the target sandwich.

The pole pieces of the spectrometer were covered by large scintillators to permit the identification and rejection of scattered events.

Figure 8 shows the focal plane counters in more detail. For mechanical reasons, the focal plane was divided into three parts, denoted as "F", "H", and "I" planes. Behind the F and H planes was placed a thickness of degrader (carbon on the F plane, aluminum behind

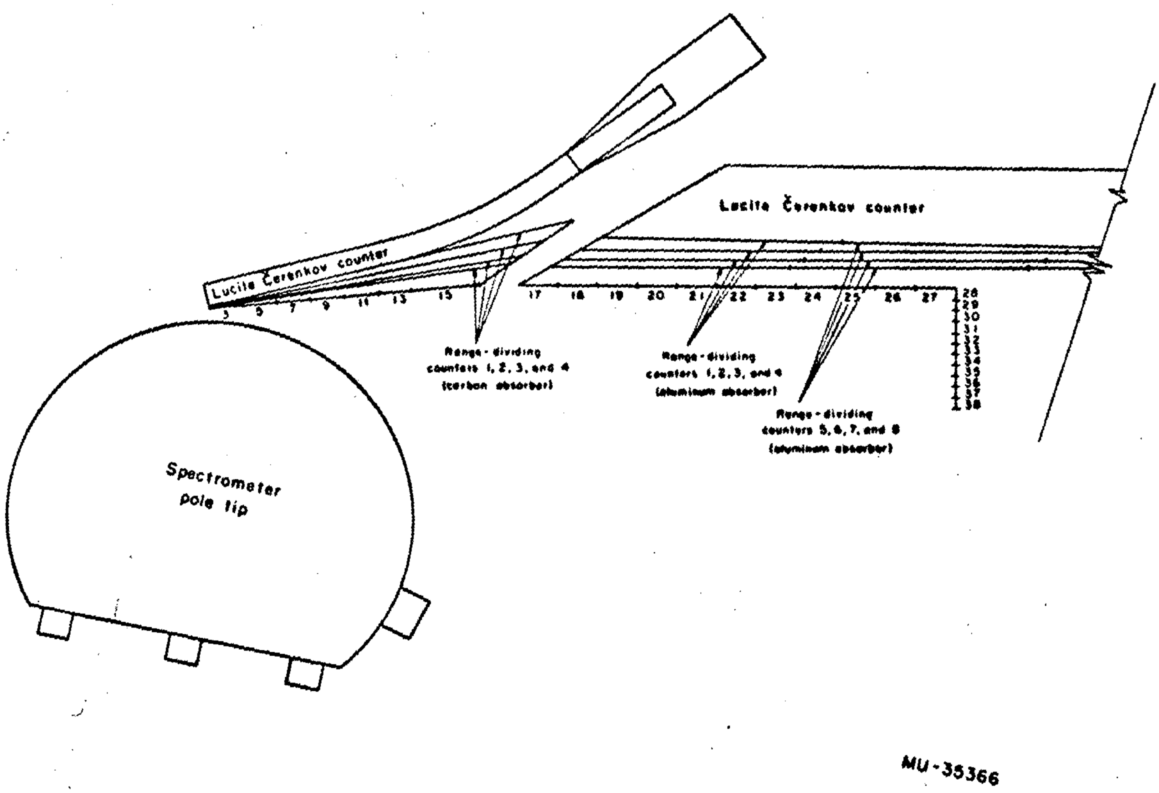

Fig. 8. Details of focal plane counter array.

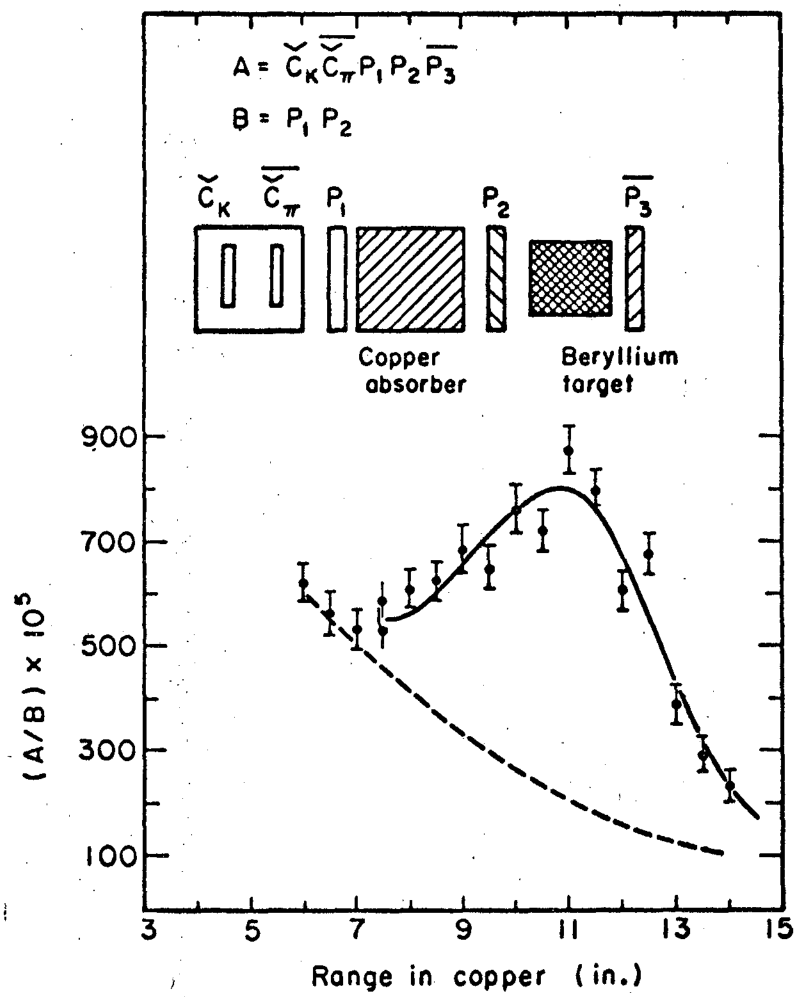

MU-35696

Fig. 9. K^+ stopping rate as function of degrader thickness.

the H plane) of a thickness sufficient to stop pions and to degrade muons below threshold for Cerenkov radiation in lucite. This degrader was followed by a two-inch-thick lucite Cerenkov counter on the F plane, and a five-inch-thick lucite Cereknov counter on the H plane. The F plane Cerenkov Counter was viewed by one RCA 7046 photomultiplier, and the H plane Cerenkov counter was viewed by five RCA 7046 photomultipliers. The carbon absorber following the F plane was subdivided into four thicknesses by four scintillation counters; the aluminum absorber behind the H plane was also subdivided into four thicknesses, by a total of eight scintillation counters. Ranges were not measured on the I plane, ($P > 230$ MeV/c). All range counters and focal plane counters shown in Figure 6 were of plastic scintillator, viewed by RCA 6810A photomultiplier tubes, as were also the B and C plane counters and the ten scintillators which subdivided the beryllium target.

E. The Orbit Tracking Program

In order to calculate solid-angle and other corrections to the data, an orbit-tracking program was written for the IBM 7094 computer. For this purpose, magnetic field measurements were made throughout the useful volume of the spectrometer, with the aid of the magnet testing group. To avoid limitations of time and core storage, these data were not used directly in tabular form in the program, polynomial fits being used instead.

1. The Quadrupole Tracking

The coordinate system is shown in Figure 6. The quadrupole was divergent in the X-Z plane, convergent in the Y-Z plane. The equations of motion, to third order in the displacements (x,y) and slopes (x',y') are[14]

$$x'' - k^2 g(z)x = k^2\left(g\frac{x}{2}(3x'^2 + y'^2) - gx'y'y - g'xyy' - \frac{g''}{12}x(x^2 + 3y^2)\right)$$
$$y'' + k^2 g(z)y = -k^2\left(\frac{gy}{2}(3y'^2 + x'^2) - gx'y'x - g'xyy' - \frac{g''y}{12}(y^2 + 3x^2)\right) \qquad [I]$$

where $k^2 = 1/(1313p)$ numerically, if $g(z)$ is specified in gauss/inch and p is in MeV/c. The primes denote differentiation with respect to z. Inside the central region of the quadrupole, $g''(z) = 0$, and $g(z)$ is just the usual quadrupole gradient: $B_x = g(0)y$, $B_y = g(0)x$. The tracking through the quadrupole proceeds as follows:

To start the solution, the equations

$$x'' - k^2 g(z)x = 0$$
$$y'' + k^2 g(z)y = 0$$

are solved. The quadrupole is treated as a succession of elementary quadrupoles, each of length one inch, with the appropriate $g(z)$. By use of the usual quadrupole transfer matrices, an approximation to the trajectory is tabulated at intervals of one inch in z:

$$\begin{vmatrix} x_{i+1} \\ x'_{i+1} \end{vmatrix} = \begin{vmatrix} \cosh\phi & \frac{\sinh\phi}{k} \\ k\sinh\phi & \cosh\phi \end{vmatrix} \begin{vmatrix} x_i \\ x'_i \end{vmatrix}, \quad \begin{vmatrix} y_{i+1} \\ y'_{i+1} \end{vmatrix} = \begin{vmatrix} \cos\phi & \frac{\sin\phi}{k} \\ -k\sin\phi & \cos\phi \end{vmatrix} \begin{vmatrix} y_i \\ y'_i \end{vmatrix}$$

where $\phi = k\sqrt{g(Z_i)}\Delta Z_i$ and where x_i means $x(z_i)$, etc., Equations [I] are now written as four first-order equations:

$$u' = k^2\left(gx + \frac{gx}{2}(3x'^2 + y'^2) - gx'y'y - g'xyy' - \frac{g''}{12}x(x^2 + 3y^2)\right) \qquad \text{IIIa}$$
$$x' = u \qquad \text{IIIb}$$
$$v' = -k^2\left(gy + \frac{gy}{2}(3y' + x'^2 - gx'y'x - g'xyx' - \frac{g''}{12}y(y^2 + 3x^2)\right) \qquad \text{IIIc}$$
$$y' = v \qquad \text{IIId}$$

[III]

Hence u_i' may be tabulated, using the first approximations to x_i, x_i', y_i, and y_i' in Equation [IIIa]. Now, u_1 is given (initial slope x'), and u_2 may be found by the trapezoidal rule:

$$u_2 = u_1 + \frac{(u_1' + u_2')}{2} \Delta Z$$

The remaining u_i may be found by Simpson integration:

$$u_i = u_{(i-2)} + \frac{\Delta z}{3} \cdot (u'_{(i-2)} + 4u'_{(i-1)} + u'_i)$$

These improved u_i's may be integrated in the same way to provide the x_i's in the second approximation. These u_i's and x_i's may now be used in equations IIIc to find improved v_i's, and so on. Three or four cycles through equations [III] are sufficient in practice; the fractional changes in the positions and slopes at the exit end of the quadrupole in the next iteration are 0.1% or less.

2. The Spectrometer Tracking Routine

Through the spectrometer, the position at any point on the trajectory is given by x, y, and z, where z is now measured from the center of the spectrometer (i.e., the origin of coordinates has been translated from the target to the center of the spectrometer, but without rotation, so that x and y are before). The direction (or vector momentum) at any point along the trajectory is specified by the projected angle in the x-z plane, (Θ) and the angle of the inclination to this plane (ψ), so that the momentum components are

$$P_x = P_{\parallel} \sin \Theta \qquad P_{\perp} = P_y$$

$$P_z = P_{\parallel} \cos \Theta \qquad P_{\parallel} = P \cos \psi$$

$$P_y = P \sin \psi \qquad P = \sqrt{P_{\parallel}^2 + P_{\perp}^2}$$

where Θ is the angle between the Z-axis and the x-z projection of the trajectory. The symmetry of the magnet allows the separation of the field into an axial (B_y) and radial (B_r) component, both functions of y and $r \sqrt{x^2 + z^2}$. In a uniform axial field, (B_y = constant, B_r = 0) the trajectory in the field region would be a helical arc of pitch angle ψ. By treating the orbit as a series of short helical arcs, the tracking routine takes the simple form* $x_{i+1} = x_i + \Delta x_i$, etc, where

$$\begin{vmatrix} \Delta x_i \\ \Delta y_i \\ \Delta z_i \end{vmatrix} = \rho \begin{vmatrix} A & 0 & B \\ 0 & \delta \tan \psi & 0 \\ B & 0 & -A \end{vmatrix} \begin{vmatrix} \cos \Theta_i \\ 1 \\ \sin \Theta_i \end{vmatrix}$$

$\rho_i \delta$ is the projected arc in the x-z plane, $\rho_i = \dfrac{1313 P_{\parallel}}{B_y(r,y)}$ is the radius of the projected arc (ρ in inches, p in MeV/c) and

$$A = 1 - \cos \delta$$

$$B = \sin \delta$$

δ may be specified in advance, so that A and B need be computed only once. The change in direction (projected) along the trajectory is simply a rotation in the plane:

$$\begin{vmatrix} \sin \Theta_{i+1} \\ \cos \Theta_{i+1} \end{vmatrix} = \begin{vmatrix} 1-A & B \\ -B & 1-A \end{vmatrix} \begin{vmatrix} \sin \Theta_i \\ \cos \Theta_i \end{vmatrix} = \begin{vmatrix} \cos \delta & \sin \delta \\ -\sin \delta & \cos \delta \end{vmatrix} \begin{vmatrix} \sin \Theta_i \\ \cos \Theta_i \end{vmatrix}$$

Where B_r is finite, the pitch angle also changes:

---

*A term proportional to $|\vec{P}_{\perp} \times \vec{B}_r|$ is neglected here, since $|\vec{P}_{\perp} \times \vec{B}_r| \ll |\vec{P}_{\parallel} \times \vec{B}_y|$ everywhere. Comparison of these orbits with others calculated without approximation shows that no appreciable error is introduced by neglecting this term. Both methods of calculation agree well with measured orbits obtained by the floating wire method.

$$\text{Tan } \psi_{i+1} = \text{Tan } \psi_i + \frac{B_r \sin \epsilon}{B_y} \times (1+\tan^2\psi_1) \text{ where } \sin \epsilon = \frac{\vec{P}_{\parallel} + \vec{B}_r}{P\ B_r}$$

$B_y(r,y)$ and $B_r(r,y)$ are computed from polynomial approximations.

3. Momentum Dependence of Solid Angle of Spectrometer

The momentum dependence of the solid angle of the magnetic spectrometer (Fig. 10) was determined by tracking a large number of orbits with the orbit tracking program. These orbits were sent into unit elements of area on the unit sphere about the source point in the target, so that all orbits had equal weight in the final summation. The source points were taken in a grid over the target volume, in order to obtain a target-averaged solid angle. The stopping distribution of K's in the target was taken to be uniform in this calculation; this is a valid approximation over the target volume contributing to the solid angle, in view of the rather broad momentum distribution of the incident K beam (see also Section III-G).

The expected range distributions of pions and muons were obtained at the same time, by following each orbit the appropriate distance into the array of counters and degraders behind the focal plane, (see Fig. 8). The pion range distributions were corrected for losses by nuclear attenuation in the aluminum absorber. A collision mean free path of 22 inches was used here, corresponding to an absorption cross section of 300 millibarns.[16] The contribution of elastic scattering to this attenuation was neglected in this calculation, since the range-dividing counters subtend most of the forward hemisphere and would therefore intercept the main elastic diffraction peak.[17] The loss of $K\pi 2$ pions by this means was calculated at 15%. This loss occurs

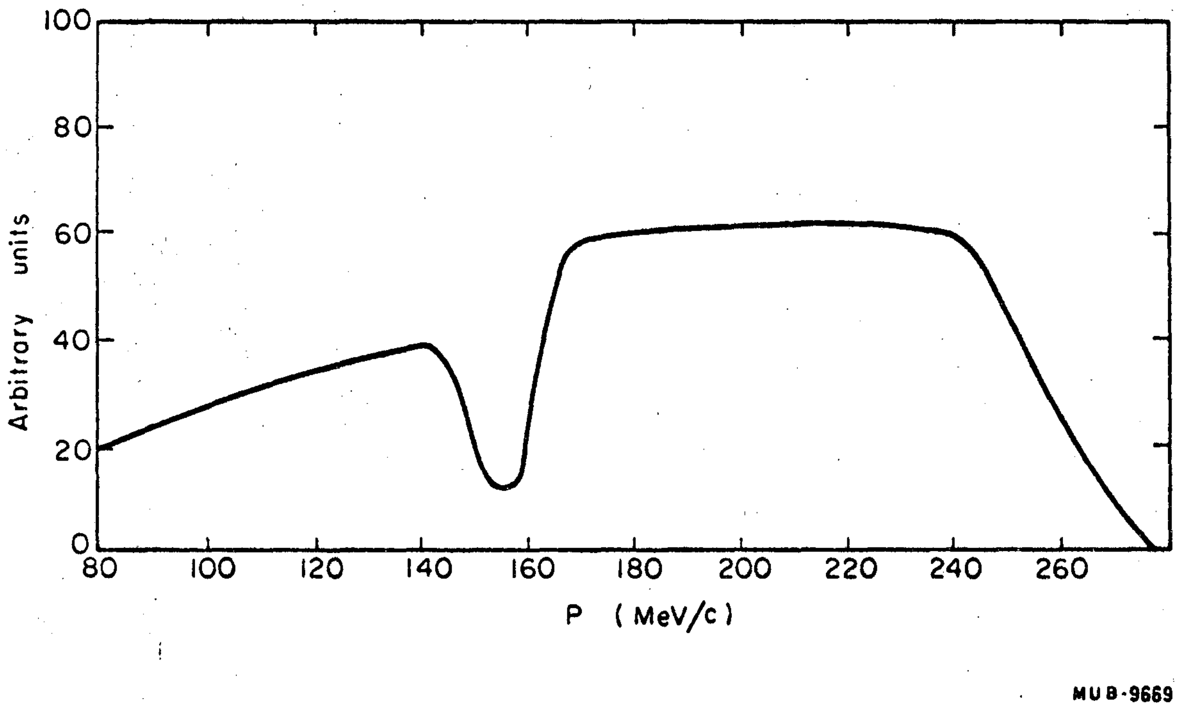

Fig. 10. Effective target-averaged solid angle of spectrometer as a function of momentum. The dip at 155 MeV/c corresponds to the gap between the F and H focal plane segments.

in the first two slabs of degrader, since events with fewer than two range counts were rejected in the data analysis, (see Section III-A).

III. DATA ANALYSIS

A. Selection Criteria

Film taken on the four-beam oscilloscope (see Section II-C) was read by film scanners and recorded on data forms. Those events meeting preliminary criteria ((a) below) were then punched on IBM cards as input to a data-sorting program written for the IBM 7090 Computer. Events meeting the following criteria were selected by the sorting program for final analysis.

a. An entrance counter sequence was present; i.e., a B plane signal, a C plane signal, and one of the nine possible target-counter sequences (A1, ALXA2, ALXA2XA3, etc.) was present, and a focal plane count (F, H, or I plane).

b. No pole-piece anti-counter signals were present. (192 rejections).

c. A coincidence with at least two range-dividing counters was required for all events on the F and H counter planes. (980 events rejected). These counters (shown in Fig. 8) were arranged so that pions would penetrate at least two, and muons and electrons would penetrate at least three. By requiring two or more range-dividing counters, background protons were rejected. Some pions were lost by nuclear absorption before attaining their normal ranges, and were therefore also rejected by this requirement. The observed $K\mu 2/K\pi 2$ branching ratio is corrected for this loss.

To eliminate film-scanning errors from the final data, all events surviving the above tests were rescanned by the senior film scanner. The final data consisted of 4852 events.

Figure 11 is a histogram of the final data, corrected for the variation of the solid angle of the spectrometer with momentum, and for momentum losses in the beryllium target. Since these losses are different for muons and pions, an average correction was used. The momentum uncertainty thus introduced is 5 MeV/c on the F plane, hence a coarse momentum interval has been taken. On the H plane the uncertainty is only 2 MeV/c, and it is completely negligible on the I plane.

An additional correction was made at each end of the spectrum, for the following reason: a particle whose momentum at point of origin in the target is above the momentum cutoff of the spectrometer may still be counted if it loses sufficient momentum in the target, while at the low momentum end a particle may be lost because its loss in the target left it below the momentum cutoff. In effect, the target volume diminishes at the ends of the spectrum. The correction is again different for pions and muons, but negligibly so at the high-momentum end. At the low-momentum end an averaged correction was used.

In the following two sections of this report we will be concerned with finding what fraction of the data of Figure 11 must be subtracted as background, and with determining the relative numbers of pions and muons in the data above 170 MeV/c. Both of these problems are greatly simplified by the fact that the K^+ decay products above 170 MeV/c consist almost entirely of $K\pi 2$ pions and $K\mu 2$ muons. The results obtained in the following two sections enable us to separate the data above 170 MeV/c essentially into three components: $K\pi 2$, $K\mu 2$, and

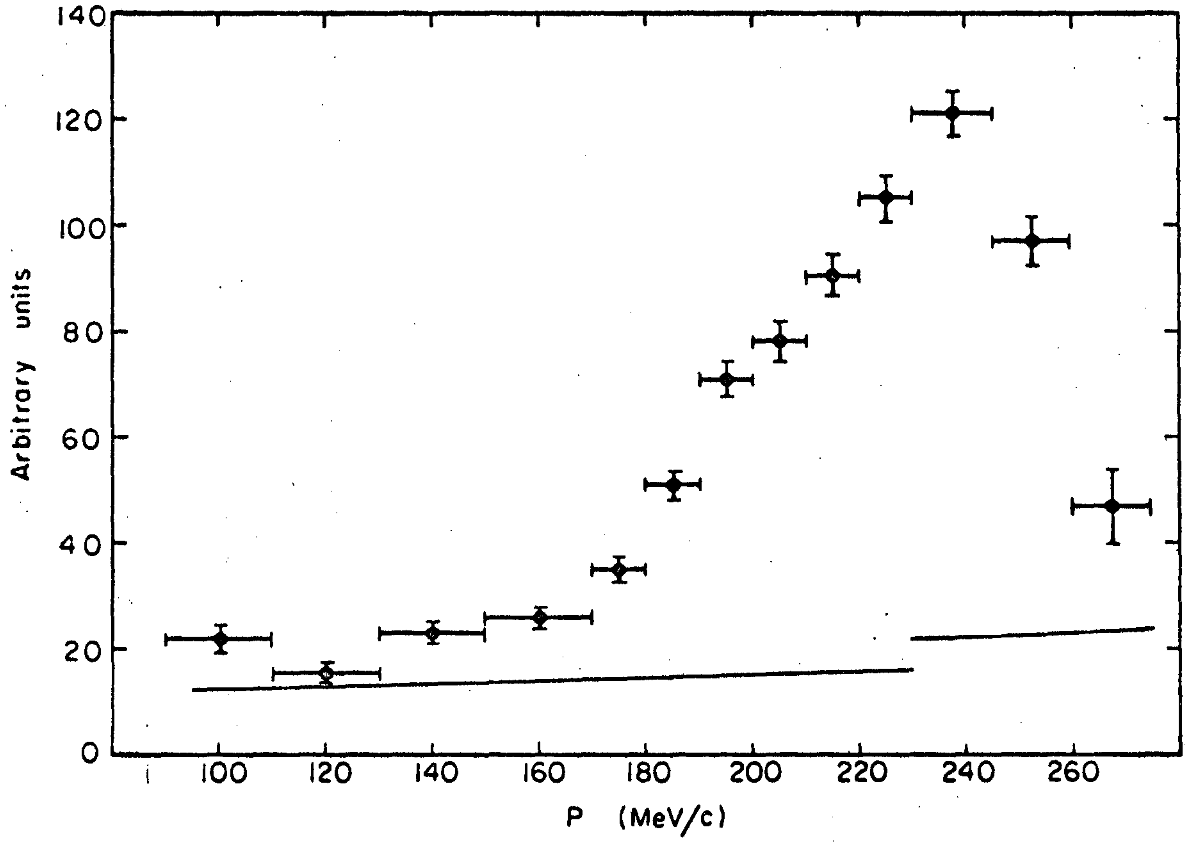

MUB-9663

Fig. 11. Total data in final sample, showing fraction of data which is subtracted as background pions.

background. The remaining sections of this report are devoted to calculation of corrections for losses of $K\pi2$ pions, and some minor contaminations to the $K\mu2$ mode.

B. Background Subtraction

From the measured integral range curve it is known that some of the "K stops" are in fact pions. These counts may be attributed to pions which traversed the beam Cerenkov counter at appreciable angles to the main beam axis (thus counting in the K channel of the Cerenkov counter) and then underwent nuclear interactions in the beryllium target, thereby missing the anti-counter behind the target. In order to determine the contamination of the K-decay spectrum arising from these pion interactions in the beryllium target, a series of background data runs was taken. These runs were taken at reduced beam, with the K and π channels of the Cerenkov interchanged; under these running conditions a pure background spectrum was obtained.

A linear least-squares fit to the background pion spectrum is shown in Figure 12. The discontinuity at 230 MeV/c results from the fact that ranges were not measured on the I plane, hence it was not possible to reject the short-range events, as was done with F and H plane data. To allow for this expected discontinuity the fitted function was taken as

$$\begin{aligned} B(p) &= (A + Mp) \qquad && p < 230 \text{ MeV/c} \\ &= T(A + Mp) && p > 230 \text{ MeV/c} \end{aligned}$$

where B(p) is the relative background intensity, A, M, and T are constants to be determined by the least-squares fit, and p is momentum.

The least-squares fit just discussed gives the form of the

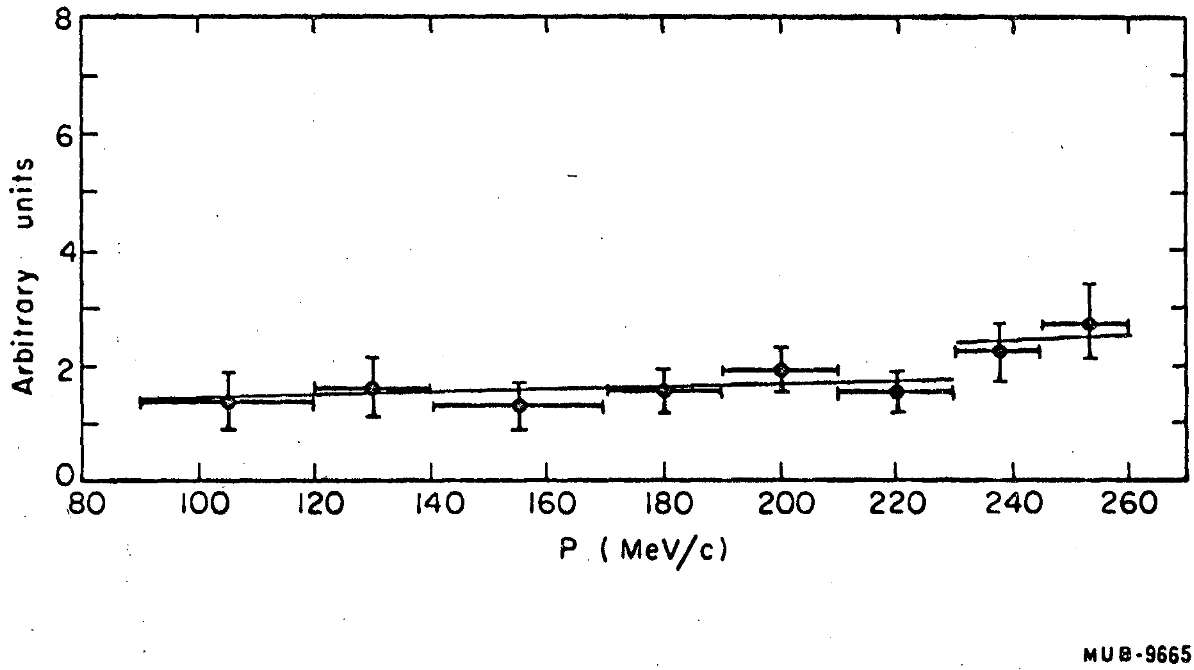

Fig. 12. Data from background runs. The line is a least-squares fit to the data.

background pion spectrum, but does not tell us how much background must be subtracted from the total data. To see how this subtraction may be made, we recall (from Table 1) that in the absence of any background the F plane data would consist of events from four three-body modes: Ke3, Kμ3, τ and τ', while the H and I plane data would consist of Kμ2, Kπ2, Ke3, and Kμ3. Other contaminations to the data (chiefly from Kπ2 pions decaying in flight) are discussed elsewhere in this report. Taking account of these decay modes, and claculated contaminations, it is found that (in the absence of background) the ratio

$$R = \frac{\text{total data on H and I plane}}{\text{total data on F plane}}$$

should be $9.2 \pm .5$. The error in R is determined by the errors in the branching ratios quoted in Table 1. The background may be subtracted now by requiring that the data remaining after subtraction satisfy the ratio R. In computing this ratio we have used weighted averages of the branching ratios quoted in Table 1; specifically the two-body sum $\overline{K\pi 2 + K\mu 2}$ and the three-body branching ratios relative to this sum. It should be noted that our use here of the Kπ2 + Kμ2 sum does not conflict with the independence of our result, since we measure the ratio Kμ2/Kπ2. The experiments of Table 1 agree within statistics on this sum, but not upon the ratio, as has already been indicated in our introduction. It should also be noted that the data on the F plane includes contaminations from the two-body modes (e.g., muons from Kπ2 pions decaying in flight) which must be normalized in this calculation to the observed Kπ2 and Kμ2 peaks. These peaks in turn are not determined until after the background has been subtracted. It was therefore necessary to iterate the solution to obtain a selfconsistent background normalization.

The (calculated) three-body spectra used in this normalization are consistent with results of recent experiments.[18,19,21] All K^+ decay components and calculated contaminations entering into the background subtraction described here are tabulated (Table III) and described in more detail in Sections III-D and III-E.

In subtracting the background in this manner, we are in effect finding a number $(N + \Delta N)$ such that when we subtract $(N + \Delta N)(B(p) \pm \Delta B(p))$ from the data of Figure 11, the remaining data satisfies the ratio R above. (B(p) is also defined above). In addition to the error in R, statistical uncertainties in our total data and background data contribute to ΔN. The error in B(p) is found from the error matrix of the least-squares fit to the background data, and includes the correlations between the parameters in this fit. Figure 13 shows the data after subtraction of the normalized background.

In the following section it will be explained how the information provided by the range sub-dividing counters behind the H focal plane was used to separate the data on this plane into pion and muon components. Together with the background normalization above, this information tells us what fraction of the data of Fig. 11 is pions, and what fraction is background. By subtraction we obtain the range-separated data of Figure 15.

C. Identification by Range

As shown in Figure 8, the F and H focal planes were backed by slabs of carbon and aluminum, respectively, separated by range-dividing scintillation counters. The observed range distributions for the H

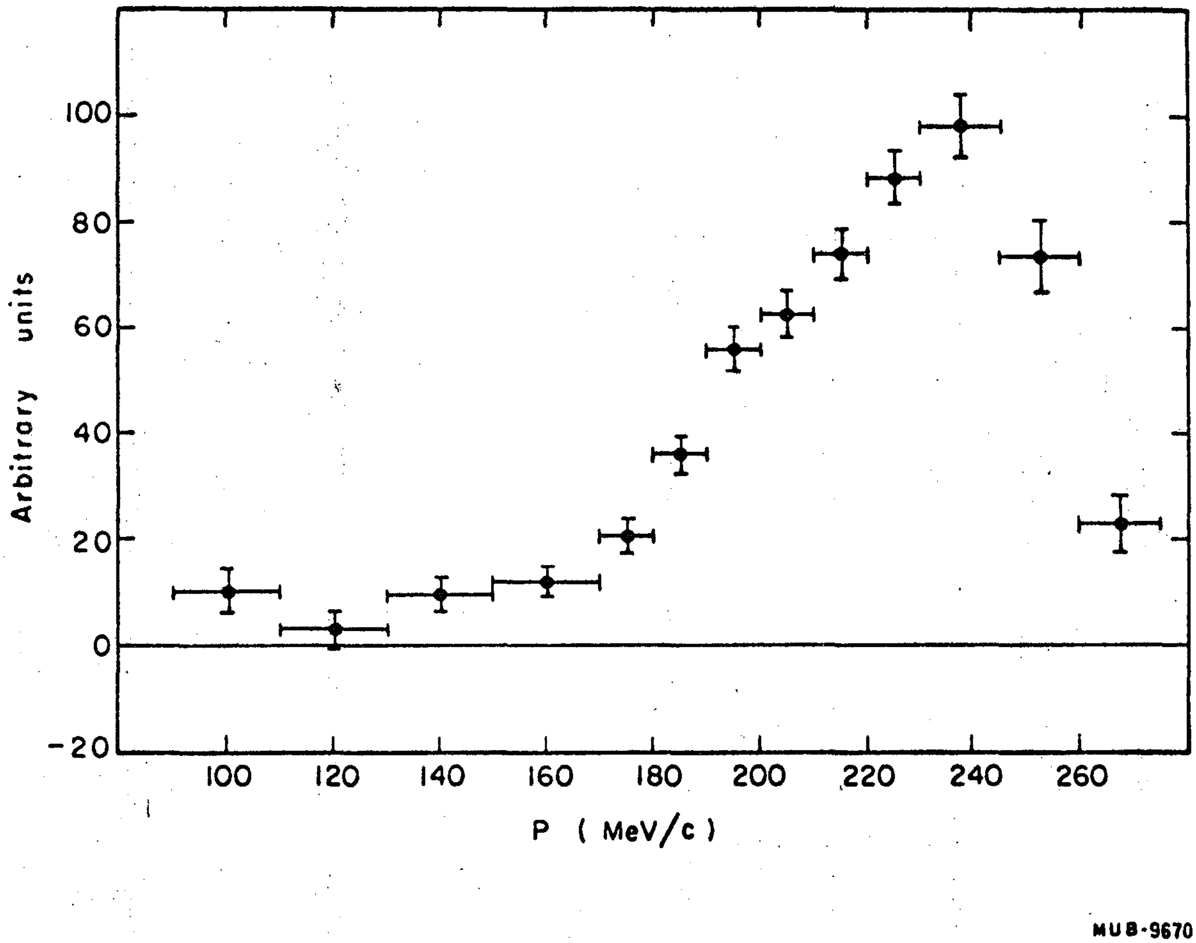

Fig. 13. Data after subtraction of background.

plane are given in Figure 14. The expected range distributions for π's and μ's were calculated with the aid of the orbit tracking program, and the observed distributions were separated into π and μ components.

The observed range distribution of each bin in Figure 14 may be thought of as a vector, $\vec{D}$, having three components, namely, the number of counts in counters RH_2, RH_3, RH_4. The range calculations indicate the pions end in range intervals RH_2 and RH_3, while muons end in the intervals RH_3 and RH_4. In the following discussion these calculated range distributions are denoted as $\vec{\pi} = (\pi_1, \pi_2, 0)$ and $\vec{\mu} = (0, \mu_2, \mu_3)$ where the subscripts 1, 2, 3, refer to range intervals RH_2, RH_3, RH_4. The fits were made by forming a comparison vector $\vec{G} = N_\pi \vec{\pi} + N_\mu \vec{\mu}$ and then finding those values of N_π and N_μ (for each of bins 17-27) which minimize the sum

$$S = \sum_{i=1}^{3} \frac{(D_i - G_i)^2}{D_i}$$

where $D_{1(2,3)}$ = number of counts in $RH_{2(3,4)}$. The minimum values of S obtained from these fits should be distributed as χ^2 for one degree of freedom. The results of these range fits are given in Table 2, which shows the fraction of counts identified by range as pions for each focal plane bin. This information permitted the separation of the data into pions and muons over the momentum interval 170-230 MeV/c, which included the range of overlap of the $K\pi2$ and $K\mu2$ modes.

Figure 15 shows the data after separation by range over the interval 170-270 MeV/c. Since the range information does not extend above 230 MeV/c, the $K\pi2$ data point at 237.5 MeV/c is extrapolated from the fit to the $K\pi2$ data, and subtracted from the total data to obtain

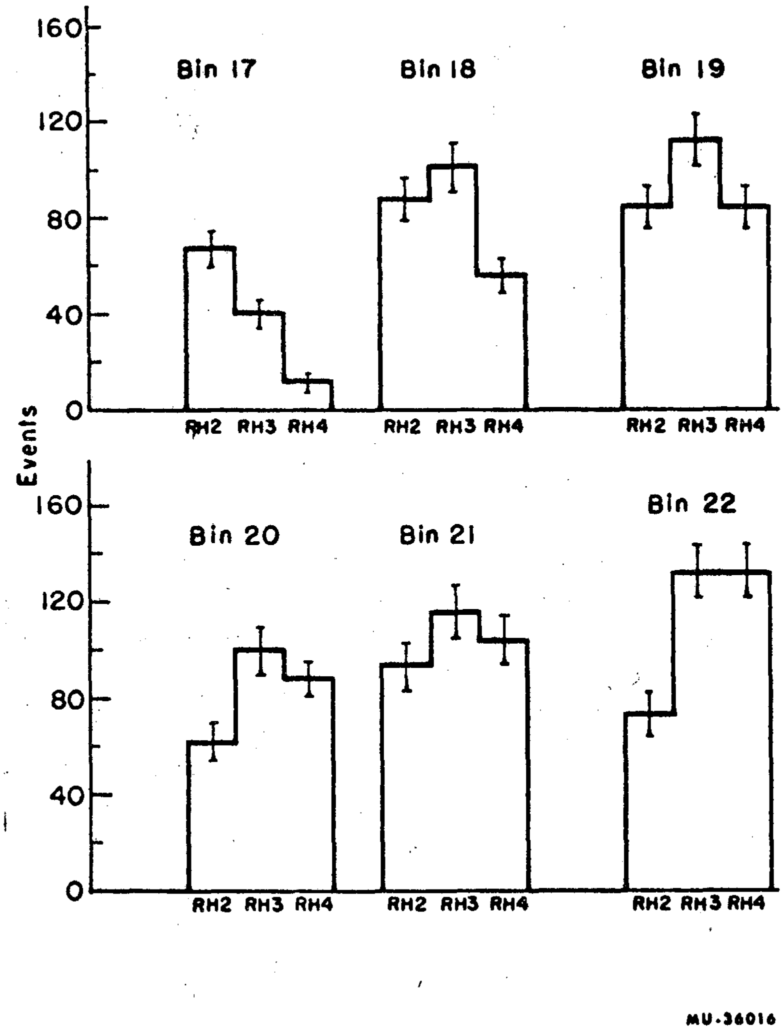

Fig. 14. Observed range distributions on the H plane. RH2 denotes the number of particles stopping between the second and third range dividing counters, RH3 is the number stopping between the third and fourth counters, and RH4 the number penetrating all four range counters. These counters are shown in Fig. 8.

Table II

$\overline{P}$(MeV/c)	Bin	$N_\pi/(N_\pi + N_\mu)$	Error	χ^2	Probability of larger dev.(1%)
157	17	.595	.048	1.17	28
167	18	.539	.076	3.94	4
176	19	.559	.036	1.04	31
183	20	.595	.034	.024	88
190	21	.629	.030	1.48	22
196	22	.566	.088	2.40	12
201	23	.497	.090	3.29	7
206	24	.347	.034	.35	55
211	25	.294	.033	.04	85
216	26	.238	.033	.10	75
221	27	.233	.035	1.01	32

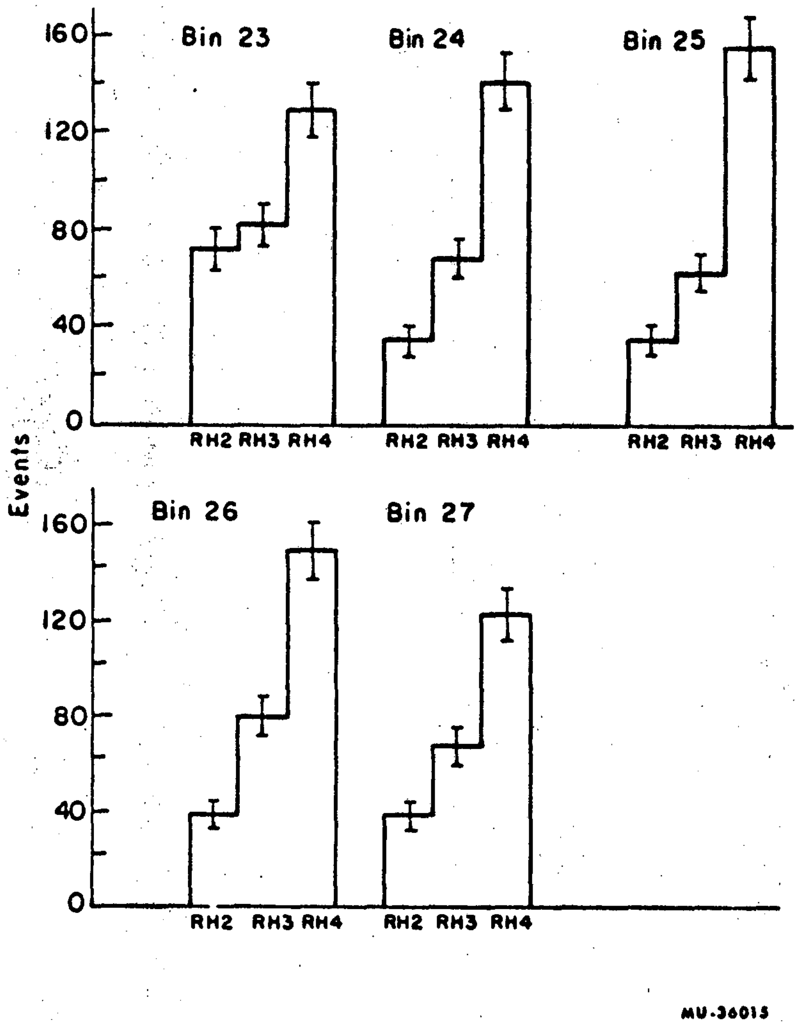

Fig. 14b. Observed range distributions on the H plane.

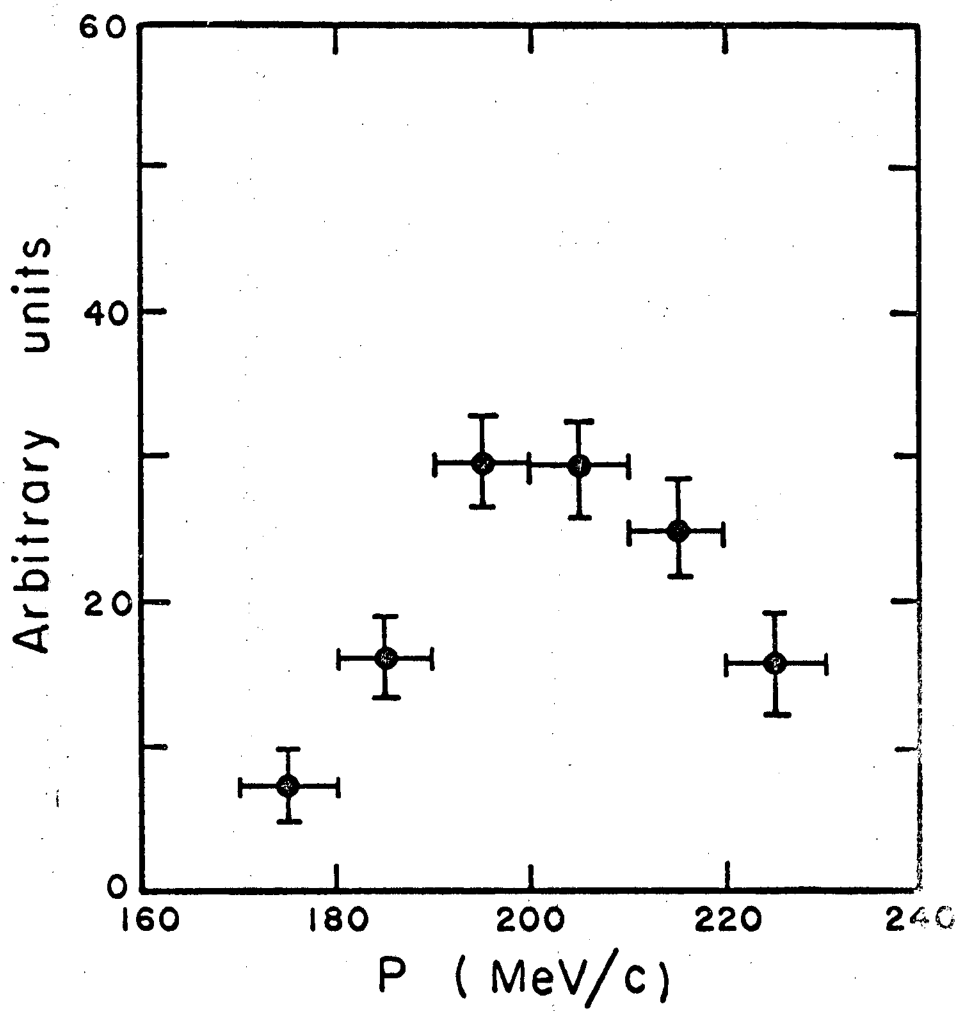

MUB-9...

Fig. 15a. Momentum distribution of particles with pion ranges.

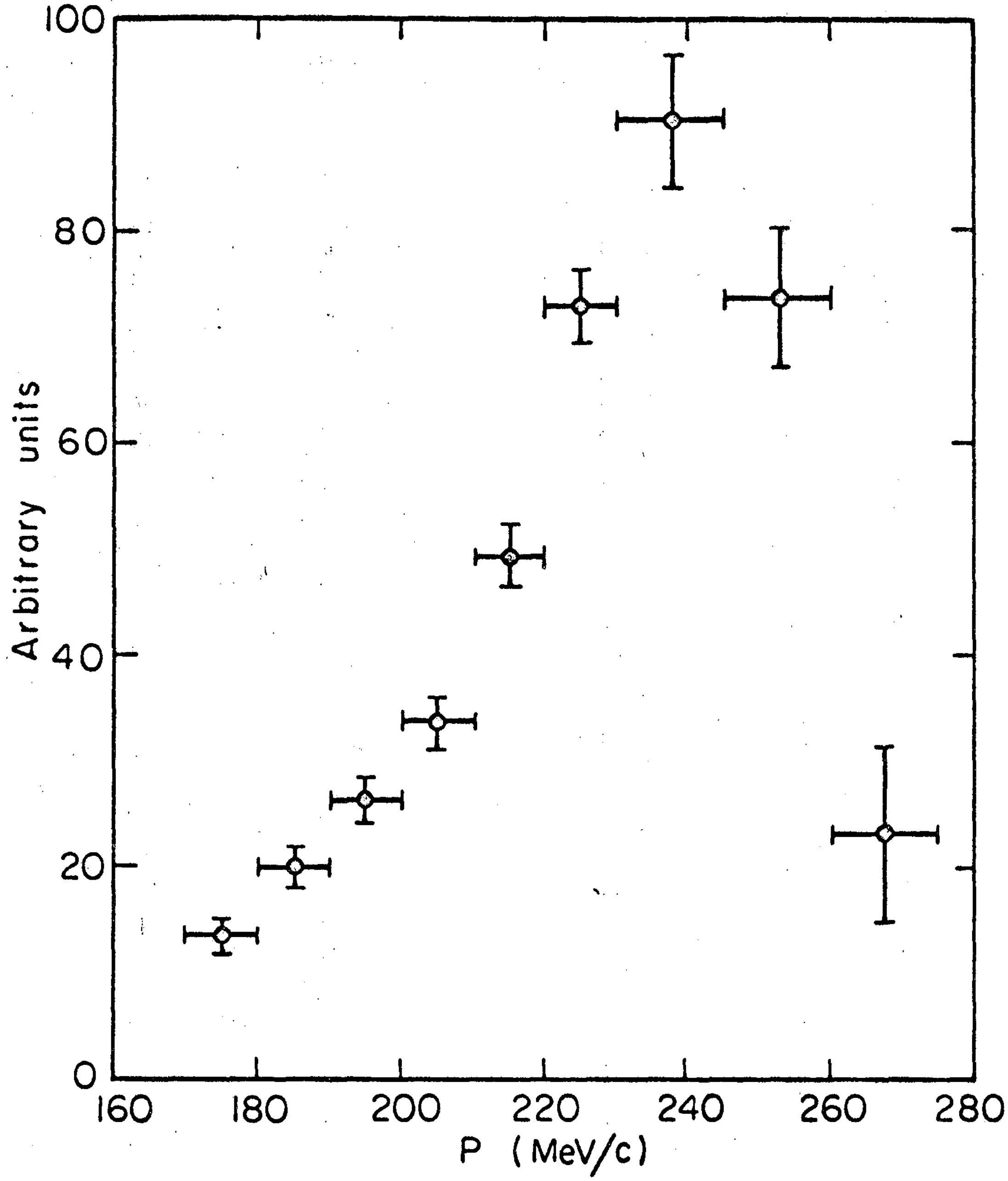

MUB-9662

Fig. 15b. Momentum distribution of particles with muon ranges.

the $K\mu2$ data point at 237.5 MeV/c.

D. Corrections to the $K\pi2$ Mode

As already noted, an appreciable fraction of pions decay in flight through the spectrometer. The correction for this loss is calculated in D-1 below. The fraction of $K\pi2$ pions decaying in flight is .24 to .26, depending upon depth of origin in the beryllium target (average loss .25). In addition to loss by decay in flight, pions are lost by nuclear attenuation in the beryllium target and in the first two slabs of aluminum range behind the focal plane. The aluminum range must be included since events with fewer than two range counts were rejected from the sample. This loss is calculated in the Section D-2, and their effect on the measured branching ratio $K\mu2/K\pi2$ is summarized in section D-3.

1. Pion Decay in Flight

The mean decay length of the $K\mu2$ muon is 4800 feet, hence the loss of muons by decays in flight in the spectrometer was negligible. However, the mean decay length for pions from the $K\pi2$ mode is only 34 feet, and 25% of these were lost by decay in flight. A fraction of the muons from these pion decays reached the focal plane, where they contributed a small tail to the $K\mu2$ peak. A description of the calculation of this muon spectrom from pion decay in given below, with a summary of the results. Before proceeding with this discussion, it should be noted that the presence of a background of scattered pions implies the presence of a muon background arising from pion decays in flight. This background muon fraction has also been calculated; it ranges from .23 to .20 of the total background across the

H plane. The momenta and angles of intersection of the muons at the focal plane are in general different from those of particles following continuous orbits through the spectrometer, and the calculation (described below) shows that most will be identified as pions by range. In subtracting the background from the range-separated data, account was taken of this muon fraction.

In order to calculate the spectrum from π decay in flight, the orbit tracking program was modified as follows. Each orbit was divided into segments of length such that the probability of pion decay along with each segment was uniform. From the center of each segment a number of equally probable muons from pion decay in flight were tracked through the remainder of the spectrometer. These orbits were confined to a narrow cone (half-angle $\simeq 12^{\circ}$) about the initial pion direction at point of decay; their momenta ranged from approximately 95 to 210 MeV/c. The expected range distributions for these muons was obtained at the same time. Some 20,000 of these decay muon orbits were tracked in this calculation.

The results of the calculation may be summarized as follows:

Twenty-five per cent of the $K\pi 2$ pions entering the spectrometer decayed before reaching the focal plane. The muons from these decays in flight may be divided into three classes:

a. Muons lost in the magnetic pole tips, or missing the focal plane counters (10%)

b. Muons reaching the focal plane with pion-like ranges (9%)

c. Muons reaching focal plane with muon-like ranges (6%)

The percentages listed are relative to 100% for the pions entering the spectrometer. 7% of the muons in class (b) fell within the $K\pi 2$ peak; the remaining 2% extended on the lower-momentum side and contributed to the F plane data.

2. Pion Losses by Nuclear Attenuation

In addition to the loss by decay in flight, pions are lost at each end of the spectrometer by nuclear attenuation. The loss in the aluminum behind the H plane was obtained as a part of the solid angle calculation (cf. Section II-E3). It was found that 15% of the $K\pi 2$ pions arriving at the focal plane were lost in aluminum. Pions are also lost in the beryllium target; in consequence of this loss the spectrometer accepts only 96% of the $K\pi 2$ mode, the remaining 4% being absorbed in the target. An absorption cross-section of 100 millibarns was used in this calculation.[16]

Elastic scattering does not contribute significantly to this attenuation.*

3. Summary of $K\pi 2$ Losses

Consideration of the $K\pi 2$ losses by decays in flight, together with the losses by nuclear attenuation leads to the following expression for the correction factor which must be applied to the observed

---

*To a good approximation, those pions which are scattered elastically out of an element of solid angle about the beryllium target are balanced by pions which scatter in. Since these pions originate from K^+ mesons decaying isotropically at rest, it is clear from symmetry that this balance would be exact if the beryllium target were spherical. For the actual target geometry used here, the elastic scattering into the spectrometer is calculated to be about 9% greater than out-scattering. If we assume that elastic and absorption cross-sections to be roughly equal, then the effect of the elastic scattering is an order of magnitude less than the (4%) effect of nuclear absorption, and is therefore neglected here.

$K\mu 2/K\pi 2$.

$$F = S_b(S_t \cdot S_a + .07)$$

where S_b is the fraction of $K\pi 2$ pions leaving the beryllium target, S_t is the fraction surviving through the spectrometer, S_a is the fraction surviving through the aluminum degrader before the range-dividing counters, and the term .07 represents those decay-like ranges which fall within the $K\pi 2$ peak. The calculated values are

$$S_b = .96$$

$$S_t = .75$$

$$S_a = .85$$

The factor F which must be applied to the observed $K\mu 2/K\pi 2$ relative branching ratio is therefore .68. The uncertainty in F is estimated to be $\pm$ .026 (see Sec. III-G).

E. Contaminations to $K\mu 2$ Mode

The $K\mu 2$ mode is subject to none of the losses affecting the $K\pi 2$ mode, but is contaminated by other decay modes to some extent. The main $K\mu 2$ peak at 236 MeV/c has a lower momentum tail consisting of (at least) the following components:

a. $K^+ \rightarrow e^+ + \pi^o + \nu$

b. $K^+ \rightarrow \mu^+ + \pi^o + \nu$

c. Those muons from $K\pi 2$ pion decay in flight which are identified by range as muons.

d. Muons from $K\mu 2$ decay in flight in beryllium target (see Sec. E2 below).

e. A scattering tail consisting of $K\mu 2$ muons which grazed the exit edges of the quadrupole singlet. This effect is discussed in

Sec. E2 below.

The contribution of the decay mode $K^+ \rightarrow \mu^+ + \nu + \gamma$ has not been considered here, but is presumably small in comparison with those components listed above. Components a. and b. can be taken from Table I, and the calculation of component c. was described in Section III-D1. The calculation of components d. and e. is discussed below.

In Figure 16 the muon data is shown as a sum of the Kμ2 peak and components a. through e. above. The Kμ2 curve is a gaussian, fitted to the data from 210 MeV/c through 270 MeV/c, and component d. and e. are normalized to this Kμ2 fit. The Ke3 and Kμ3 components are those predicted by the V-A theory of weak interactions; their branching ratios are taken as 5% and 3.5% respectively (cf. Table I) and in the Kμ3 spectrum the form factor $\xi = f-/f+$ was taken to be zero, which is consistent with recent experiments.[18,19] The momentum resolution of the spectrometer has been folded into the predicted Kμ3 and Ke3 here. Table 3 summarizes these contributions to the Kμ2 tail.

1. Scattering in Quadrupole Edges

The orbit tracking program previously discussed was also used to compute the expected Kμ2 and Kπ2 tails arising from scattering in the edges of the quadrupole singlet at the entrance to the spectrometer. To this program was added a subroutine in which those particle orbits which intersected a quadrupole boundary were tracked through a simulated scattering and ionization loss process. Each trajectory within the scattering material was stepped off in short segments of length $\Delta_i = S_{i+1} - S_i$ where S is measured along the trajectory. The direction is specified in standard spherical coordinates in which

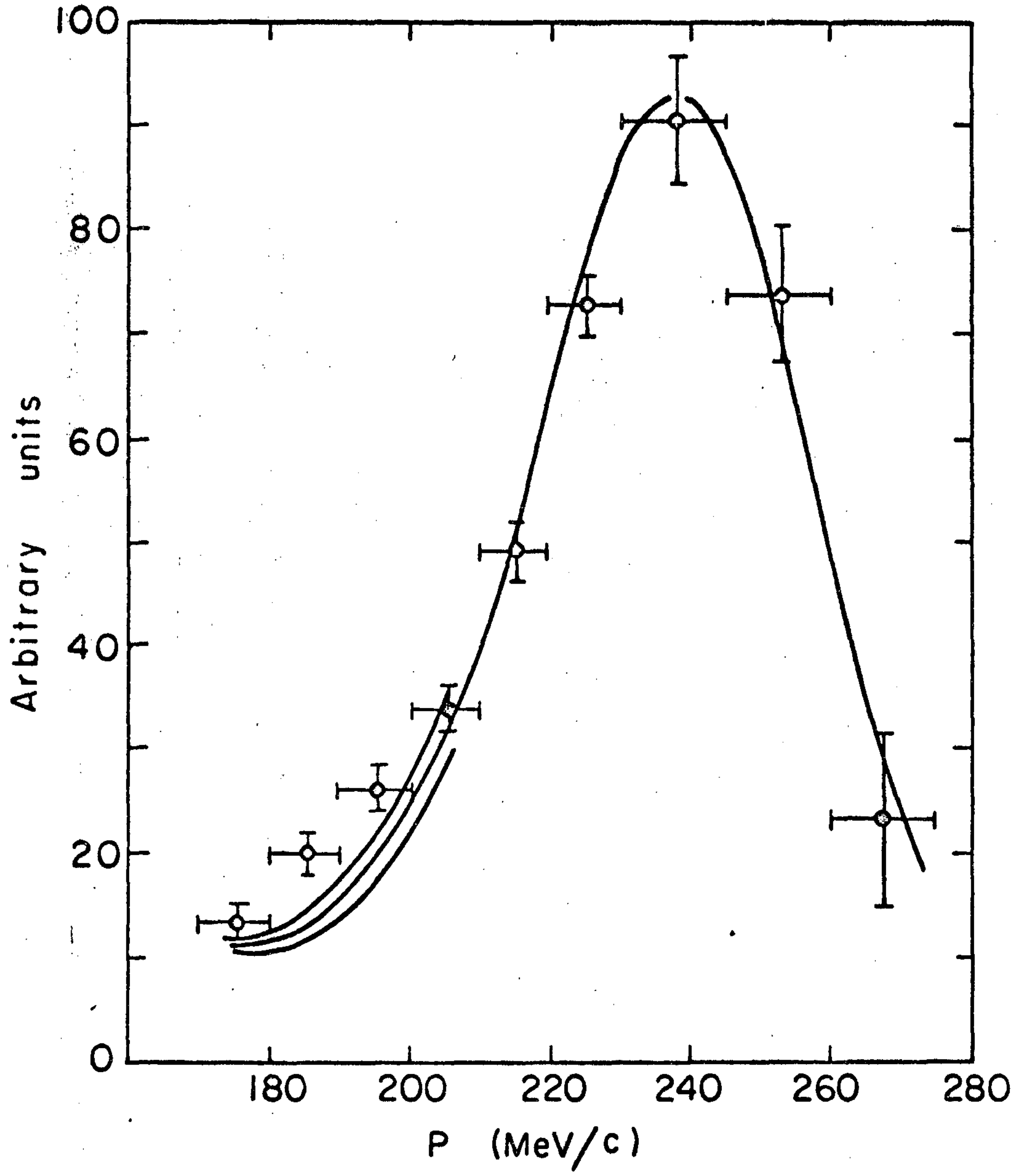

Fig. 16. Fit (including calculated contaminations) to the muon data. Table III lists the components of the fitted curve.

Table 3

PC	τ,τ'	Ke3	$K\mu3$	π_μ	K_π	K_μ	S_π	S_μ	$K_{\mu2}$	$K_{\pi2}$
95	.97	2.48	1.80	.05				.12		
105	2.60	2.76	2.01	.12			.10	.38		
115	3.08	2.99	2.18	.37			.22	.49		
125	1.88	3.18	2.32	.59			.32	.65		
135	.63	3.76	2.35	.68			.39	.65		
145	.09	3.28	2.32	.68	.38		.46	.77		
155		3.21	2.20	.69	.76		.51	1.04		
165		3.03	1.99	1.01	1.27	.10	.70	1.19		
175		2.75	1.68	1.57	1.77	1.33	1.01	1.37		7.63
185		2.36	1.27	1.88		2.58		2.08		17.07
195		1.16	.77	2.10		3.71		3.50	8.21	27.14
205		1.27	.26	1.88		4.65		4.96	22.90	31.07
215		.61		1.07					48.39	25.45
225		.07		.42					74.26	14.92
237.5									90.02	
252.5									70.71	
267.5									29.02	

S_π, S_μ = Quadrupole edge scattering, normalized to observe $K\pi2$, $K\mu2$ peaks

K_π, K_μ = $K\pi2$, $K\mu2$ decays in flight

π_μ = $K \rightarrow \pi^0 + \pi^+ \rightarrow \mu + \nu$ in flight

$K\mu2$, $K\pi2$ (fits to data of Figures 15a and 15b)

τ,τ', Ke3, $K\mu3$ are calculated from branching ratios of Table I, and normalized to $\Sigma(K\pi2 + K\mu2)$ above the z axis is taken along the direction of motion, Θ_i is the polar angle, and ϕ_i the azimuthal angle. At the end of each segment the momentum of the particle is reduced by $\Delta_i \cdot \frac{dp}{dx}(P_i)$ and a new direction Θ_{i+1}, ϕ_{i+1} is specified by choosing two random numbers; ϕ_{i+1} is taken from a uniform distribution over the interval 0-2π, and Θ_{i+1} from a gaussian distribution of width

$$\overline{\Theta}(p_i) = \frac{21.2}{P_i\beta_i}\sqrt{\frac{\Delta_i}{x_o}}$$

where x_o is the radiation length in the medium. The trajectory is followed in this manner until either the momentum of the particle has fallen below the cutoff momentum of the spectrometer, or the particle re-enters the spectrometer, in which case the usual tracking is resumed. The results of this calculation are summarized in Figure 17.

In order to consider the effect of scattering in the pole tips of the quadrupole, it is useful to think of the Kμ2 and Kπ2 quadrupole scattered components as consisting of two parts, one of which falls within the main peak and is therefore indistinguishable from it, and another which falls outside and appears as a "tail". The part of the scattered component which falls within the main peak may be regarded simply as equivalent to a small fractional increase fπ(fμ) in the acceptance solid angle. The tail itself does not enter directly into the measurement of the branching ratio. (Both tails add to the F plane data, however, and were therefore considered in the background subtraction.) The net effect of this scattering is therefore to introduce a factor $(1+ f_\mu)/(1+ f_\pi)$ into the observed branching ratio

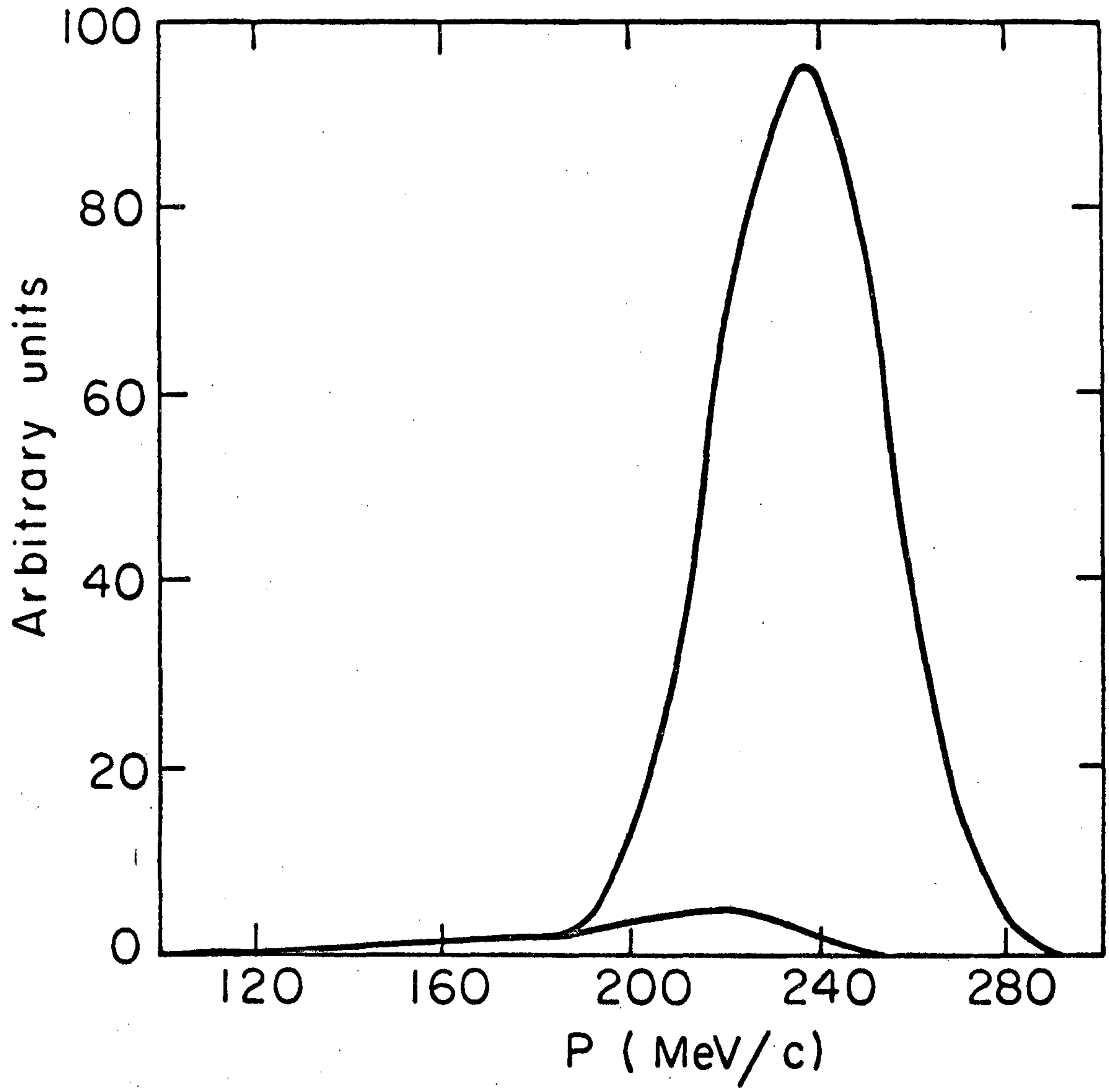

MUB-9664

Fig. 17. Calculated tail on Kμ2 peak from Kμ2 muons which scattered in edges of quadrupole. The Kπ2 tail is similar.

$K\mu2/K\pi2$ as estimated from the main $K\mu2$ and $K\pi2$ peaks. Here f_μ and f_π are the fractional increase in solid angle for the $K\mu2$ muon and the $K\pi2$ pion, respectively. It is found that the net effect on the $K\mu2/K\pi2$ ratio is largely self-cancelling; i.e., $f_\mu \simeq f_\pi \simeq .04$. The resulting tails are given in Table 3.

2. Decay in Flight Corrections - K^+

An appreciably fraction of K^+'s decayed in flight within the beryllium target. The effect of these decays is to degrade the momentum of the decay particle which enters the spectrometer, hence to provide lower momentum tails to the $K\pi2$ and $K\mu2$ peaks. A rough estimate of this effect can be obtained at once. The mean K momentum incident on the beryllium target is 350 MeV/c, corresponding to a range of 4 inches in beryllium. The K meson traverses the first 3-1/2 inches of its range with an average velocity $\overline{\beta} \simeq 0.5$ and hence requires 0.6 nanoseconds to approach within 1/2 inch of the end of its range. (Decays within the last 1/2 inch are indistinguishable from decays at rest, within the momentum resolution of the spectrometer.) The fraction of incident K's decaying in flight then is

$$1 - \exp\,(t/\tau) \simeq t/\tau = 0.6/14. = .04$$

where $\tau = \dfrac{12.2 \text{ ns}}{\sqrt{1-\overline{\beta}^{\,2}}}$ is the K mean life. We may therefore expect that some 4% of the K decays will be in flight. Since the angular distribution of the charged products of these decays is peaked in the beam direction, the acceptance of the spectrometer (at 90° to this direction) for these products is less than for decays at rest. Hence we have the inequality

$$\underset{(K\pi2)}{K\mu2 \text{ tail}} < 0.04 * \underset{(K\pi2)}{K\mu2 \text{ peak}}$$

Because of the close similarity between the $K\pi 2$ and $K\mu 2$ tails these K decays in flight have no direct effect on the measurement of the $K\mu 2/K\pi 2$ relative branching ratio. Since the $K\pi 2$ tail extends onto the lower focal plane, it is considered in the background normalization. The calculation will now be described in more detail.

The broad-range spectrometer selects particles leaving the beryllium target at approximately 90° to the incident K beam (Fig. 1). The probability that the spectrometer will accept the muon from a $K\mu 2$ decay in flight between depths $(y, y + dy)$ in the beryllium target is proportional to

$$\sigma_{90}(p_k')\Delta\,\Omega(y)$$

where $\sigma_{90}(p_k')$ is the decay angular distribution function, evaluated at 90° in the lab system, and $\Delta\Omega(y)$ is the acceptance solid angle of the spectrometer seen from depth y in the target, evaluated at the appropriate muon momentum. Strictly, $\Delta\Omega$ is a function of x, y, and z. The integration described here is done with x_i and z_i fixed, then a summation over x_i and z_i is performed.

The decay angular distribution function and the mean decay length of the K meson at depth y in the target are functions of its momentum p_k' at that point, or, equivalently, functions of y and initial momentum P_i through the relation

$$p_k'(y) = P_k - \int_0^y \left(\frac{dP}{d\zeta}\right) d\zeta$$

The distribution $W(P_k)$ of incident K momenta may be estimated from the K differential range curve (Fig. 9).

The momentum distribution of muons from these decays in flight may be written in the form of a histogram:

$$\int_{P_\mu^i}^{P_\mu^{i+1}} N(P_\mu)\, dP_\mu \sim \int_{P_k^i}^{P_k^{i+1}} W(P_k) dP_k \int_{y_i}^{Y_{i+1}} \sigma_{90}(p_k')\Delta\,\Omega(y) S(P_k,y)\, \frac{dy}{\lambda(p_k')}$$

Here $S(P_k,y) = \exp\left(-\int_0^y \frac{d\zeta}{\lambda(P_k,\zeta)}\right)$ is the probability that the K meson has survived to depth y, and $S(P_k,y)\frac{dy}{\lambda(p_k')}$ is the probability that a K meson of incident momentum P_k will decay between y and y + dy in the target.

The momentum of a decay muon coming off at 90° from a K of velocity β' is

$$P_\mu = P^* \sqrt{1 - \left(\frac{\beta'}{\beta^*}\right)^2}$$

where P^* and β^* are the muon momentum and velocity in the K^+ rest frame.

The angular distribution function may be written as

$$\sigma_{90}(P_k') \sim \sqrt{(1 - \beta'^2)(1 - (\frac{\beta'}{\beta^*})^2)}$$

The integrals in y and P_k are taken over these ranges which contributes to the decay muon momentum interval $P_\mu^{i+1} - P_\mu^i$.

In order to normalize this computed decay muon spectrum to the $K\mu 2$ peak from K decays at rest, the following integral, corresponding to K decays at rest, was also calculated:

$$\int W(P_k)\, dP_k \left[S(P_k,y)\Big]_{y=R} \cdot \Delta\Omega(y)\Big]_{y=R} \right]$$

where $S(P_k,y)$ and $\Delta\Omega(y)$ are evaluated at that depth R in the target which corresponds to the range of a K meson of momentum P_k.

A similar calculation was made for $K\pi 2$ decay mode; the results of both calculations are given in Table IV. Because of their small branching ratios, the effect of K decays in flight upon Ke3 and Kμ3 modes was not considered. The Kπ2 and Kμ2 tails from this effect are given in Table 3.

F. Relative Branching Ratio Kμ2/Kπ2

The relative branching ratio Kμ2/Kπ2 is derived directly from the gaussian histograms which are fitted to the data of Figure 15. These fitted curves were of the form

$$f(P) = \frac{N}{\sqrt{2\pi}\sigma} \exp\left(-1/2 \left(\frac{P-\overline{P}}{\sigma}\right)^2\right)$$

The parameters N, σ, and $\overline{P}$ are those which minimize the sum

$$S = \sum_i \left(\frac{Y_i - \overline{Y_i}}{e_i}\right)^2$$

a minimum.

Here Y_i is the data point, e_i its associated error, and

$$\overline{Y_i} \quad \int f(P)\, dp$$

where the integral extends over the momentum interval centered at p_i. This observed ratio must be scaled by the factor .68 to account for the losses of pions by nuclear attenuation and decay in flight, as discussed in Section III-D.

The results of these fits are given in Table 4.

Table 4

	$K\pi 2$	$K\mu 2$
N	1338. ± 104.	4538. ± 243.
σ	16.8 ± 1.6 MeV/c	19.5 ± 1.3 MeV/c
$\overline{P}$	204.0 ± 1.5 MeV/c	237.8 ± 1.1 MeV/c

The position of the $K\mu 2$ and $K\pi 2$ peaks may be computed from the masses of the particles involved; the $K\pi 2$ pion has a momentum of 205 MeV/c, and the $K\mu 2$ muon momentum is 236 MeV/c. The values obtained in Table 4 are seen to be consistent.

The observed branching ratio is accordingly

$$\frac{N\mu}{N\pi} = \frac{4538 \pm 243}{1338 \pm 104} = 3.39 \pm .32$$

The corrected relative branching ratio is

$$K\mu 2/K\pi 2 = (.68 \pm .03)(3.39 \pm .32)$$
$$= 2.31 \pm .24$$

where we have used the results of section III-G in assigning an error of .03 to the pion loss factor.

G. Uncertainties in Calculated Corrections

It will be recalled that the factor .68 is applied to the observed $K\mu 2/K\pi 2$ ratio to compensate for loss of pions by decays in flight and nuclear absorption. It was shown in Section III-D3 that this factor has the form

$$F = S_b(S_t S_a + .07)$$

where

$$S_b = \exp\,(-\overline{X}/\lambda)_{AL}$$

where λ now is the mean absorption length in aluminum, and $\overline{X}$ is the thickness of aluminum degrader between the focal plane and the range-dividing counters

$$S_t = \exp\,(-L/\lambda) \text{ where } \lambda + \beta\gamma c\tau_\pi$$

is the mean decay length of the $K\pi 2$ pion, and L is the length of its orbit through the spectrometer. Appropriately weighted averages of all these parameters were used in calculating S_b, S_t and S_a. The calculation of S_t involves only the mass and lifetime of the pion, and the dimensions of the spectrometer. The uncertainties in these parameters are small in comparison with those in the absorption cross-sections, and may be neglected here. To see this we note that the mean decay length of the pion may be written as

$$\lambda = \frac{P_\pi c\tau_\pi}{m_\pi} \quad (P_\pi \text{ in MeV/c, } m_\pi \text{ in MeV})$$

Now,[20]

$$m_\pi = 139.580 \pm .015 \qquad (.01\% \text{ uncertainty})$$

$$\tau_\pi = 2.551 \pm .026 \qquad (1\% \text{ uncertainty})$$

Hence

$$\frac{\Delta\lambda}{\lambda} = \frac{\Delta\tau_\pi}{\tau_\pi} \simeq 1\%$$

Then

$$\frac{\Delta_{St}}{S_t} = \frac{L}{\lambda}\,\frac{\Delta\lambda}{\lambda} = (.29)(.01) = 0.3\%, \text{ which is negligible.}$$

fidence) with the results of Shaklee et al., and inconsistent with Roe et al.

IV. ACKNOWLEDGEMENTS

It is my pleasure to thank Professor Kenneth M. Crowe for his interest and active participation in this experiment. I would also like to take this opportunity to thank the many people without whose help and participation this experiment would have been impossible. Dr. Hans Kruger designed the counter array and other equipment associated with the magnetic spectrometer. Dr. Tin Maung designed the K^+ secondary beam.

In addition to those already mentioned, Professor Roy P. Haddock, Mr. Philip Beilin, Mr. Ned Dairiki, and Dr. Robert Shafer all participated actively in the experiment. I also wish to thank Mr. David Schwartz and Mr. James Shilleto for capable and energetic assistance with the programming of numerical work, and Mr. Patrick Craig for assuming chief responsibility for film scanning.

The K^+-selecting Cerenkov counter was kindly loaned by Professor Owen Chamberlain.

V. REFERENCES

1. W. Becker, M. Goldberg, E. Hartle, J. Kitmer, and S. Lichtman, Nuovo Cimento 31, 1 (1964).
2. R. W. Birge, D. H. Perkins, J. Peterson, D. H. Stork, and M. W. Whitehead, Nuovo Cimento 4, 834 (1956).
3. G. Alexander, R. Johnston, and C. O'Cealliagh, Nuovo Cimento 6, 478 (1957).
4. S. Taylor, G. Harris, J. Orear, J. Lee, and P. Baumel, Phys. Rev. 114, 359 (1959).
5. B. P. Roe, D. Sinclair, J. L. Brown, D. A. Glaser, J. A. Kadyk, and G. H. Trilling, Phys. Rev. Letters 7, 346 (1961).
6. F. S. Shaklee, G. L. Jensen, B. P. Roe, and D. Sinclair, Phys. Rev. 136, B1423 (1964).
7. I. Goldberg and L. Landowitz, Nuovo Cimento 21, 869 (1961).
8. A. E. Everett, Phys. Rev. Letters 14, 615 (1965).
9. Lawrence Radiation Laboratory Counting Handbook, UCRL-3307 Revised June 5, 1964.
10. T. A. Nunamaker, Engr. Note EE-783, Lawrence Radiation Laboratory (1961).
11. C. P. Browne and W. W. Buechner, Revs. Sci. Instr. 27, 899 (1956).
12. H. A. Enge, Revs. Sci. Instr. 29, 885 (1958).
13. R. L. Burman and A. I.Yavin, Nuclear Instruments and Methods 7, 101 (1960).
14. A. Septier, P. Grivet, Nuclear Inst. 6, 243 (1960).
15. R. M. Sternheimer, Phys. Rev. 130, 511 (1956). Range table incorporating Sternheimer's corrections for the density effect are given

in Methods of Experimental Physics, Part A, Academic Press, 1961 and Techniques of High Energy Physics, Interscience, 1961, D. M. Ritson.

16. P. Huguenin, Zeits. for Physik, 167, 416 (1962).

17. T. A. Fujii, Phys. Rev. 113, 695 (1959). W. F. Baker, J. Rainwater, R. E. Williams, Phys. Rev. 112, 1763 (1958). W. F. Baker, H. Byfield and J. Rainwater, Phys. Rev. 112, 1773 (1958).

18. G. L. Jensen, F. S. Shaklee, B. P. Roe and D. Sinclair, Phys. Rev. 136, 1431 (1964).

19. A. C. Callahan, U. Camerini, R. D. Hantman, R. H. March, D. L. Murphree, G. Gidal, G. E. Kalmus, W. M. Powell, C. L. Sandler, R. T. Pu, S. Natali and M. Vallani, UCRL-16593, January 3, 1966.

20. A. Callahan and D. Cline, Phys. Rev. Letters 15, 129 (1965).

21. G. Borreani, G. Rinaudo and A. E. Werbrouck, Phys. Letters 12, 123 (1964).